RICE UNIVERSITY

High Resolution Microendoscopy for Quantitative Diagnosis of Esophageal Neoplasia

by

Dongsuk Shin

A THESIS SUBMITTED
IN PARTIAL FULFILLMENT OF THE
REQUIREMENTS FOR THE DEGREE

Doctor of Philosophy

APPROVED, THESIS COMMITTEE:

Rebecca Richards-Kortum, Stanley C. Moore Professor
Bioengineering

Tomasz S. Tkaczyk, Assistant Professor
Bioengineering, Electrical and Computer Engineering

Richard G. Baraniuk, Victor E. Cameron Professor
Electrical and Computer Engineering

Sharmila Anandasabapathy, Associate Professor
Gastroenterology, The Mount Sinai Medical Center

HOUSTON, TEXAS
APRIL 2013

ABSTRACT

High Resolution Microendoscopy for Quantitative Diagnosis of Esophageal Neoplasia

by

Dongsuk Shin

Esophageal cancer is the eighth most common cancer in the world. Cancers of the esophagus account for 3.8% of all cases of cancers, with approximately 482,300 new cases reported in 2008 worldwide. In the United States alone, it is estimated that approximately 18,000 new cases will be diagnosed in 2013, and 15,210 deaths are expected. Despite advances in surgery and chemoradiation therapy, these advances have not led to a significant increase in survival rates, primarily because diagnosis often at an advanced and incurable stage when treatment is more difficult and less successful. Accurate, objective methods for early detection of esophageal neoplasia are needed.

Here, quantitative classification algorithms for high resolution miscroendoscopic images were developed to distinguish between esophageal neoplastic and non-neoplastic tissue. A clinical study in 177 patients with esophageal squamous cell carcinoma (ESCC) was performed to evaluate the diagnostic performance of the classification algorithm in collaboration with the Mount Sinai Medical Center in the United States, the First Hospital of Jilin University in China, and the Cancer Institute and Hospital, the Chinese Academy of Medical Science in China. The study reported a sensitivity and specificity of 93% and

92%, respectively, in the training set, 87% and 97%, respectively, in the test set, and 84% and 95%, respectively, in an independent validation set. Another clinical study in 31 patients with Barrett's esophagus resulted in a sensitivity of 84% and a specificity of 85%. Finally, a compact, portable version of the high resolution microendoscopy (HRME) device using a consumer-grade camera was developed and a series of biomedical experimental studies were carried out to assess the capability of the device.

Acknowledgements

I would like to thank my advisor, Dr. Rebecca Richards-Kortum, for her guidance during the past six years. Her vision, insight, and encouragement have made many things possible that would not otherwise be so.

Many thanks to the other members of my committee: Dr. Tomasz Tkaczyk for his expertise in optical instrumentation; Dr. Richard Baraniuk for his expertise in image analysis; Dr. Sharmila Anandasabapathy for leading the clinical team and keeping our focus on the clinical environment.

I would like to thank current and former members of the Kortum Lab for their help and support, including Dr. Mark Pierce, Dr. Veronica Leautaud, Dr. Darren Roblyer, Dr. Timothy Muldoon, Dr. Kelsey Rosbach, Dr. Nadhi Thekkek, John Wright, Vivian Mack.

At the Mount Sinai Medical Center, Dr. Marion-Anna Protano and Dr. Michelle Lee performed clinical measurements. Dr. Alexandros Polydorides reviewed pathology slides. Josephine Mitcham coordinated studies.

At the U. T. M. D. Anderson Cancer Center, Dr. Ann Gillenwater and Dr. Manoop Bhutani performed clinical measurements. Dr. Michelle Williams reviewed pathology slides. Tao Le, Viji Bhattar, Jency George coordinated studies.

Most importantly, I would like to express my greatest thanks to my family.

Table of Contents

1. INTRODUCTION

1.1 Objective and Specific Aims

During endoscopic examination of the esophagus, lesions which appear to be suspicious are biopsied and then examined histologically. Although patients with esophageal cancer benefit from endoscopic screening, this procedure fails to detect many esophageal cancers. High-resolution optical imaging techniques have the potential to improve diagnostic accuracy to detect pre-cancerous and cancerous lesions by visualizing subcellular changes of tissue. Confocal endomicroscopy has demonstrated the capacity to provide high-quality imaging; however, use of this technique requires expensive and complex hardware and specialized equipment. In contrast, high-resolution microendoscopy provides subcellular imaging through a fiber-optic bundle and uses a wide-field epifluorescence arrangement instead of point scanning, which reduces system complexity and cost. The objective of this research is to develop a portable, cost-effective, high-resolution microendoscope and quantitative analysis criteria for the diagnosis of esophageal neoplasia and to evaluate its diagnostic potential in clinical studies.

The specific aims of this research are:

1) Develop an automated analysis algorithm for high-resolution microendoscopic images for the quantitative diagnosis of esophageal squamous neoplasia, and evaluate its diagnostic performance through a multicenter, in vivo clinical study. The clinical study will be performed at the Mount Sinai Medical Center in the United States, the First

Hospital of Jilin University in China, and the Cancer Institute and Hospital, the Chinese Academy of Medical Science in China.

2) Develop quantitative analysis criteria based on high-resolution microendoscopic images for the detection of esophageal Barrett's neoplasia, and evaluate their diagnostic accuracy through a prospective study. The clinical study will be performed at the Mount Sinai Medical Center.

3) Design and construct a portable, cost-effective, high-resolution microendoscope using a consumer-grade camera, and evaluate its performance through a series of experimental studies.

1.2 Overview

This dissertation describes the development of quantitative classification algorithms for high resolution microendoscopy for diagnosis of esophageal neoplasia and the development of a compact high resolution microendoscope using a comsumer-grade camera. The dissertation is organized as follows.

Chapter 1 lists the specific aims of the research and provides a brief overview of the topics to be discussed.

Chapter 2 provides background information on esophageal cancer, progression of esophageal cancer, methods for detection and diagnosis, and optical diagnostic techniques. Confocal endomicroscopy and high resolution microendoscopy for diagnosis of esophageal cancer are reviewed.

Chapter 3 describes a clinical study of the diagnostic performance of a quantitative classification algorithm in 177 patients with esophageal squamous cell carcinoma. The development of an automated diagnostic algorithm is described.

Diagnostic performance is evaluated in a training set and test set, and in an independent validation set. Optimum features for diagnostic classification are identified.

Chapter 4 describes a clinical study of the diagnostic performance of a quantitative classification algorithm in 31 patients with Barrett's esophagus. The development of an automated diagnostic algorithm is described. Diagnostic performance is evaluated using sequential classification analysis. Optimum features for diagnostic classification are identified..

Chapter 5 describes the design and construction of a compact, portable HRME device. Evaluation of its performance through a series of experimental studies.is described.

Chapter 6 summarizes the results of the various studies and concludes with a discussion of the status of high resolution microendoscopy for diagnosis of esophageal neoplasia.

Chapter 7 lists references cited.

2. BACKGROUND

2.1 Motivation and significance

Esophageal cancer is the sixth most common cause of cancer-related mortality worldwide [1, 2]. Despite advances in chemoradiation therapy, the 5-year survival rate remains at a dismal 15%, primarily due to diagnosis at an advanced and incurable stage [3]. Indeed, survival rates drop dramatically once the tumor has breached the mucosal layer, reinforcing the importance of early detection.

While the disease carries a significant global burden (including in the United States), certain geographic areas, such as Iran, Central Asia, and northern China, have a particularly high incidence of esophageal squamous cell carcinoma (ESCC). The reasons for this are multifactorial, and many social and environmental factors have been implicated, including smoking, alcohol consumption, low socioeconomic status, thermal injury/hot beverage consumption, and nutritional deficiencies [2]. In northern China, age-standardized incidence rates exceed 100/100,000 per year [2, 4], making it an ideal setting for evaluation and intervention. In these regions, screening and surveillance practices have been implemented with limited success, and the incidence-to-mortality ratio still remains a grim 1:1 [5]. On the other hand, esophageal adenocarcinoma (EAC) arising in Barrett's esophagus (BE) is more prevalent in the Western World, especially in the United States, and has a fast growing incidence rate, with an estimated 600% increase from 1975 to 2001 [1-3].

Although a combination of early diagnosis through endoscopic surveillance and improved treatments at an early stage increases the 5-year survival rate of EAC to 80%,

most cases are diagnosed at an advanced stage when treatment is challenging because symptoms tend to manifest late and current detection methods have limitations [6, 7].

2.2 Progression of esophageal neoplasia

Normal esophageal tissue is characterized histologically with hematoxylin and eosin (H&E) staining by stratified squamous epithelium, as shown in Figure 1a. Esophageal neoplasia mostly falls into either ESCC or EAC. There are major differences between the two in terms of progression. ESCC is preceded by dysplasia and EAC is preceded by BE.

ESCC is believed to develop through a sequence of dysplastic precursor lesions, beginning with mild, moderate, and then severe dysplasia, carcinoma in situ (CIS), and finally ESCC, as shown in Figure 1 [8, 9]. Squamous dysplasia, which is the most well-described risk factor for ESCC, is characterized by the presence of loss of normal cell polarity, abnormal tissue maturation, and nuclear atypia, such as enlargement, pleomorphism, and hyperchromasia in the lower one-third (mild; Figure 1b), in the lower two-thirds (moderate; Figure 1c), or in all the thirds (severe; Figure 1d) of the epithelium. Squamous carcinoma in situ is characterized by the presence of dysplastic squamous cells throughout the full thickness of the epithelium, as shown in Figure 1e. Squamous cell carcinoma is characterized by the presence of neoplastic squamous cells invading the basement membrane, as shown in Figure 1f.

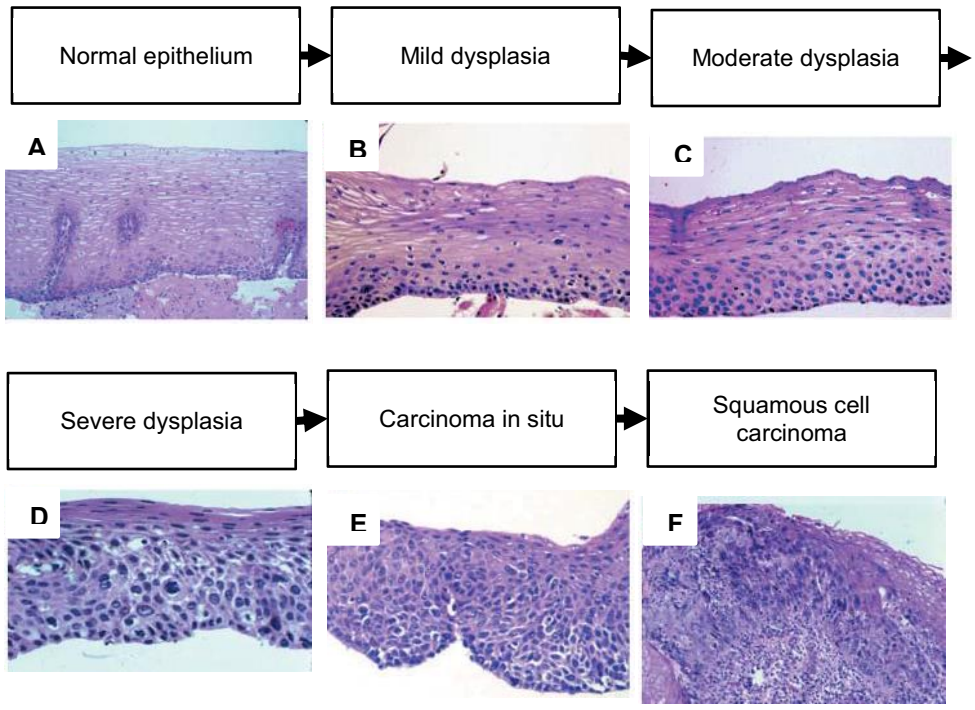

Figure 1. Progression of (a) normal squamous epithelium to (b) mild dysplasia, (c) moderate dysplasia, (d) severe dysplasia, (e) carcinoma in situ, and (f) squamous cell carcinoma.

In contrast, EAC typically arises in BE, which is characterized by the transformation of squamous epithelium to intestinal metaplasia near the gastroesophageal junction and is often caused by gastroesophageal reflux disease. This intestinal-type epithelium progresses sequentially from metaplasia, low-grade dysplasia, high-grade dysplasia, and finally to EAC, as shown in Figure 2 [10, 11]. BE is confirmed histologically by the identification of goblet cells within glands (Figure 2a). Low-grade dysplasia, which is difficult to distinguish from non-dysplastic BE, is characterized by nuclear crowding and some loss of nuclear polarity (Figure 2b). High-grade dysplasia is characterized by the overall loss of nuclear polarity and glandular structure, nuclear and glandular crowing, and especially the absence of goblet cells (Figure 2c). EAC is characterized by abortive formation of glands (Figure 2d).

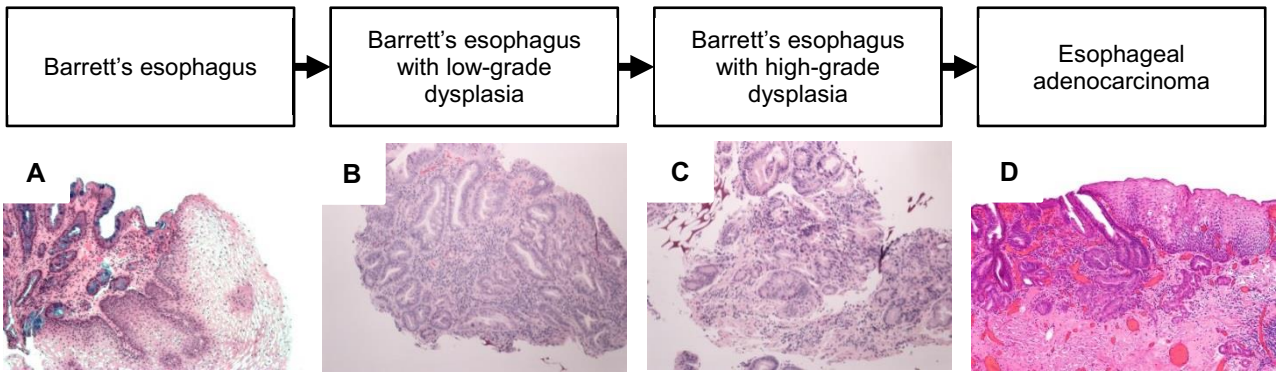

Figure 2. Progression of (a) Barrett's esophagus to (b) low-grade dysplasia, (c) high-grade dysplasia, and (d) adenocarcinoma.

2.3 Current and emerging methods for screening and diagnosis

To date, endoscopic screening with Lugol's iodine is widely used to detect squamous neoplasia, with targeted biopsy of unstained (abnormal) areas [12-14]. Typically, screening is performed in patients considered "high risk", i.e., those with a history of head and neck malignancy, positive balloon cytology, and who live in high-prevalence regions such as northern China, Central Asia, and Iran [2]. While Lugol's chromoendoscopy can highlight large areas that need further evaluation, it is limited by its poor specificity [15-17]. Indeed, inflammation and other abnormalities may often mimic neoplasia, leading to high false false-positive rates. Other novel "wide-field" imaging modalities, such as autofluorescence imaging and narrow-band imaging, have been proposed as "red flag" techniques but are less sensitive than Lugol's staining [16] and limited by high false-positive rates due to their low spatial resolution [17]. As a result, several unnecessary biopsies are taken, resulting in an increase in cost and risk.

Endoscopy with random four-quadrant biopsies for surveillance of BE with or without dysplasia is the accepted method for screening esophageal adenocarcinoma [18,

19]. However, since a segment of BE can range from 1 to 20 cm, systematic, four quadrant biopsies at 2-cm intervals leave the majority of the BE epithelium untested and can miss dysplasia and early cancer, which are often focal, flat, and not visible on routine endoscopy [20].

Advances in optical imaging techniques have facilitated efforts to utilize these techniques for diagnostic guidance of different pathological conditions. In particular, high-resolution optical imaging techniques have the potential to improve diagnostic accuracy to detect precancerous and cancerous lesions by visualizing subcellular changes of tissues in patients with esophageal neoplasia. These techniques include confocal endomicroscopy and fiber-optic high-resolution microendoscopy.

Confocal laser microendoscopy provides subcellular views of the esophageal epithelium and the ability to differentiate esophageal neoplasia from benign esophageal mucosa, with high diagnostic accuracy during endoscopy in near real time [21-31]. Previous studies have shown the ability of the confocal laser endomicroscope to successfully detect ESCC in vivo during endoscopy, allowing microscopic examination throughout the esophagus [21-24]. Deinert et al. investigated the capability of a confocal laser endomicroscope system to identify changes in the microvascular architecture of esophageal squamous epithelium in a patient with ESCC [21]. In a study by Liu et al. [22], confocal laser endomicroscopy was used to characterize alterations in cells and intrapapillary capillary loops in normal and ESCC. Diagnostic accuracy in distinguishing cancerous from normal epithelium was examined in 64 sites from 57 patients, resulting in a sensitivity of 79.4% and a specificity of 90%. In a pilot study of 43 sites from 21 patients [23], Iguchi et al. demonstrated that confocal microscopy could identify

esophageal squamous neoplasia by characterizing cellular and vascular patterns; a sensitivity of 100% and 88%, and a specificity of 94% and 90% were achieved by two endoscopists, respectively. Pech et al. examined 43 sites from 21 patients with suspected ESCC using a confocal laser microendoscope [24]. Suspicious areas identified by chromoendoscopy with Lugol's iodine were investigated using confocal imaging. All 27 neoplastic sites were diagnosed correctly and 2 of 16 non-neoplastic sites were diagnosed falsely as neoplastic, resulting in a sensitivity of 100% and a specificity of 87.5%.

Studies of patients with BE have also reported promising results with the use of confocal microendoscopy [25-31]. Kiesslich et al. [25] showed that confocal microendoscopy detected BE and BE-associated neoplasia, with a sensitivity of 98.1% and 92.9%, respectively, and a specificity of 94.1% and 98.4%, respectively, by identifying cellular and vascular changes in the BE epithelium. Pohl et al. [26] evaluated the use of confocal endomicroscopy in the detection of neoplasia in 296 sites from 38 patients with BE. Confocal imaging criteria for advanced BE neoplasia were first established in 95 sites from 15 patients, and were then tested on 201 sites from 23 patients without visible mucosa abnormalities. The results showed a sensitivity of 80% and a specificity of 94.1%, with a corresponding negative predictive value of 98.9%. Similarly, Gaddam et al. [27] established confocal imaging criteria for dysplastic BE using 50 confocal images and then evaluated accuracy and interobserver agreement using 70 testing confocal images. The sensitivity and specificity in diagnosing dysplasia were 76% and 85%, and the interobserver agreement among six endoscopists was substantial ($\kappa = 0.61$). In a study involving 11 expert endoscopists [28], Wallace et al. performed a preliminary evaluation of confocal laser endomicroscopy in a training and validation set

of 20 BE images, and yielded a sensitivity of 88% and a specificity of 96%. The study reported substantial interobserver agreement of the confocal endomicroscopy diagnosis (86%; $\kappa = 0.72$). In a prospective, randomized, double-blind, controlled, crossover study of 39 patients [29], confocal laser endomicroscopy with targeted mucosal biopsy was shown to improve the diagnostic yield of BE-associated neoplasia compared to standard endoscopy with a four-quadrant, random biopsy (33.7% vs. 17.2%). In an international multicenter, prospective, randomized, controlled study of 101 patients [30], Sharma et al. demonstrated that confocal endomicroscopy coupled with high-definition white-light endoscopy (HD-WLE) dramatically improved the ability to detect BE-associated neoplasia. Sensitivity was higher with the combination compared to HD-WLE alone (68.3% vs. 34.2%), while specificity was slightly lower (87.8% vs. 92.7%).

However, although confocal microendoscopic imaging has been shown to have the potential to significantly improve detection of esophageal neoplasia, current confocal platforms are expensive, thus making this technology only available to tertiary referral centers.

Fiber-optic high-resolution microendoscopy (HRME), an alternative to confocal endomicroscopy, has also been used to detect esophageal neoplasia in previous studies [32-36]. Muldoon et al. investigated the feasibility of HRME to image a variety of esophageal tissue types, including squamous tissue, BE, and neoplastic tissue obtained by endoscopic resection [33]. In a small pilot study of 9 patients with BE, Muldoon et al. demonstrated that HRME imaging could distinguished neoplastic from non-neoplastic tissue, with a sensitivity of 87% and a specificity of 85% [34]. In an in vivo case study of a patient with BE, Pierce et al. showed the ability of HRME to distinguish high-grade

dysplasia from normal squamous mucosa and BE without dysplasia [35]. Recently, Vila et al. assessed accuracy and interrater agreement in identifying BE-associated neoplasia using 40 HRME images from 28 patients [36]. A sensitivity of 90% and a specificity of 82% were achieved, and no significant differences in accuracy were found between experts and novices ($\kappa = 0.56$). HRME imaging also provides a relevant subcellular structure established for confocal microendoscopy and the ability to distinguish between esophageal neoplasia and benign esophageal mucosa, with high diagnostic accuracy during endoscopy. This low-cost (<$5,000) system may be useful as an adjunct to standard endoscopy in the screening and surveillance of esophageal neoplasia in a low-resource or community-based setting.

3. ANALYSIS OF HIGH RESOLUTION MICROENDOSCOPIC IMAGES FOR AUTOMATED DIAGNOSIS OF ESOPHAGEAL SQUAMOUS CELL CARCINOMA[a]

[a]The contents of this chapter are being prepared for submission to the journal The Journal of National Cancer Institute with the following author list: Shin D, Protano M-A, Polydorides AD, Dawsey SM, Pierce MC, Kim MK, Schwarz RA, Quang T, Parikh N, Bhutani MS, Zhang F, Wang G, Xue L, Wang X, Xu H, Anandasabapathy S, Richards-Kortum RR (2013)

Abstract: High resolution microendoscopy is an optical imaging technique with the potential to improve the accuracy of endoscopic screening for esophageal squamous neoplasia. In this study we developed quantitative image analysis criteria for the evaluation of neoplastic and non-neoplastic squamous esophageal mucosa. Patients undergoing standard upper GI endoscopy for screening or with known esophageal lesions were additionally imaged in vivo using high resolution microendoscopy. A total of 375 sites in 177 patients were imaged and analyzed. Quantitative information from the high resolution images was used to develop an automated algorithm to identify high-grade squamous dysplasia or invasive squamous cell cancer and compared to histopathology as the gold standard. Optimal performance was obtained using mean nuclear area as the basis for classification, resulting in sensitivities and specificities of 93% and 92% in the training set, 87% and 97% in the test set, and 84% and 95% in an independent validation set, respectively. This study demonstrates that high resolution microendoscopy with automated image analysis can aid in the identification of esophageal squamous neoplasia.

4.1 Introduction

There is an urgent global need to improve early diagnosis of esophageal squamous cell carcinoma (SCC) [1, 2, 37]. The five-year survival rate of esophageal SCC in the United States is only 19%, primarily because diagnosis is often at an advanced and incurable stage [38]. In low-resource settings, the five-year survival is much lower; for example, in Golestan Province, Iran, it is 3.4% [39]. At present, the most widely used and most sensitive method of endoscopic screening for squamous neoplasia involves Lugol's iodine staining of the esophagus with targeted biopsy of areas that do not retain dye [22-24]. However, specificity of Lugol's chromoendoscopy is poor [32-34]. Areas of inflammation often appear indistinguishable from superficially invasive carcinoma, leading to high false positive rates. Confocal microendoscopy, a high resolution imaging technique which evaluates the epithelium at 1100x magnification, has revolutionized endoscopic surveillance for neoplasia by allowing detection at the subcellular level [22, 23]. When confocal imaging is paired with Lugol's chromoendoscopy, accuracy rates have been shown to rise to nearly 95% with a dramatic improvement in specificity [24]. However, existing platforms are both expensive ($150,000-$300,000) and available only in a handful of tertiary centers worldwide.

Thus, there remains an important need for easily accessible complementary high resolution imaging technologies that can improve the accuracy of Lugol's by enhancing specificity, reducing the false positive rate, and reducing the number of biopsies needed for accurate patient diagnosis. In particular, there is a need for low cost imaging platforms that are robust, accurate, and reproducible when used in lower resource settings where there is frequently a shortage of healthcare providers. For this purpose, we

recently developed a fiber-optic high resolution microendoscope (HRME). The HRME provides images of the surface epithelium with similar resolution to confocal microendoscopy, but with significantly reduced system complexity and cost [32]. Recent studies conducted with the HRME demonstrated that sub-cellular resolution morphology can be used to detect neoplastic lesions in patients with Barrett's esophagus [33, 34], breast carcinoma [40], cervical carcinoma [41, 42] and oral squamous cell carcinoma [43].

The goal of the present study was to develop quantitative HRME image analysis criteria for the delineation of neoplastic and non-neoplastic squamous esophageal mucosa. In an ongoing clinical trial, HRME images were obtained during white light and Lugol's chromoendoscopy from areas deemed endoscopically normal, indeterminate and suspicious for neoplasia. Quantitative image analysis was used to develop an automated algorithm which was optimized using data from a training set, and the accuracy of the algorithm was evaluated relative to the reference standard of histopathology using data from independent test and validation sets. Features used in the automated algorithm were also used to develop guidelines for the visual interpretation of HRME images in vivo.

3.2 Methods

3.2.1 Patients

Study participants previously scheduled to undergo screening for ESCC or surveillance for known squamous cell dysplasia underwent standard white light upper GI endoscopy with Lugol's Iodine. Written informed consent was obtained from each subject. The study was reviewed and approved by the Institutional Review Boards at The

First Hospital of Jilin University in China, The Cancer Institute at The Chinese Academy of Medical Sciences in China, The Mount Sinai Medical Center, and Rice University.

The endoscopist recorded the location and level, and clinical impression of each Lugol's unstained area. Lugol's negative areas that were indeterminate or suspicious for neoplasia were then further interrogated with a high resolution micro-endoscope (HRME); the fiber-optic HRME system is described in detail below. Prior to HRME imaging at each site, a topical solution (1- 2 ml) of 0.01% proflavine (P2508, Sigma-Aldrich, St. Louis, MO) in sterile phosphate buffered saline was applied to the esophageal surface using a spray catheter; proflavine, which was used under an Investigational New Drug (IND) application from the Food and Drug Administration (IND 102 217), is a fluorescent contrast agent which stains cell nuclei [44]. The esophagus was rinsed with saline (1-2 ml) and residual liquid on the surface was suctioned. Following application of proflavine, the fiber-optic probe of the HRME was immediately inserted through the biopsy channel of the endoscope and the distal tip was placed in gentle contact with the mucosal surface. Real-time imaging was performed; at each site between 1 and 113 video sequences of approximately 1-3 seconds duration were acquired and were stored as movie files. HRME images were also obtained from two Lugol's stained ("normal") areas from each patient. At each site imaged with the HRME, the fiber probe was used to make a superficial dimple to "mark" the imaged area for later biopsy. Each imaged site was then biopsied and submitted for routine histologic diagnosis. All of the specimens were processed and sectioned in a standardized manner. Slides were later reviewed by two expert gastrointestinal pathologists (AP, SD) blinded to the endoscopists' clinical impressions and to the HRME images. Diagnosis was

performed using standard histologic criteria [45]; based on histologic diagnosis, samples were divided into the following categories: normal, inflammation, low-grade dysplasia (LGD), moderate-grade dysplasia (MGD), high-grade dysplasia (HGD), or cancer. Sites with discrepant diagnoses were reviewed by both pathologists to reach consensus. Sites initially diagnosed as moderate-grade dysplasia were later re-reviewed independently by both pathologists, and consensus was reached to diagnose these sites as either LGD or HGD depending on whether dysplasia was confined to the lower 1/2 of the epithelium (LGD) or not (HGD).

3.2.2 Imaging System

The HRME system has been described in detail previously [46]. Briefly, the system acquires fluorescence images via a coherent fiber bundle placed in contact with the tissue surface to be imaged. Illumination is provided via a bandpass-filtered blue light-emitting diode (LED) (FF01-452/25, Semrock, Rochester, NY; M455L2, Thorlabs, Newton, NJ). Light is reflected at a dichroic mirror (485DCLP, Chroma Technology Corp, Bellows Falls, VT) onto a 1 mm outer diameter fiber bundle (FIGH-30-850N, Fujikura, Tokyo, Japan), which is comprised of 30,000 optical fibers with a center-to-center spacing of 4 μm and a 720 μm field of view (FOV). Fluorescence emission returning through the fiber bundle is imaged through the dichroic mirror and a 550 nm bandpass filter (FF03-550/88, Semrock, Rochester, NY) onto the optical sensor of a CCD camera (GRAS-14S5M, Point Grey, Richmond, Canada). The lateral and axial resolution of the system are 4.4 and 20 μm, respectively. The system is controlled by a laptop computer which acquires and displays video at a frame rate of 15 frames per second.

3.2.3 Automated Image Analysis

Videos acquired with the HRME were reviewed for quality control (QC) purposes by three observers (RRK, MP, MAP) who were blinded to clinical impression and pathologic diagnosis. First, one reviewer (MP) identified a single representative image frame from each video sequence. Selected images were then reviewed for QC independently by all three reviewers. Images were rejected if at least 50% of the FOV was out of focus, showed evidence of motion artifact, or was obscured by debris at the tip of the fiber bundle. At each site, images which met the QC process were then reviewed to select the single image with the highest visual image quality.

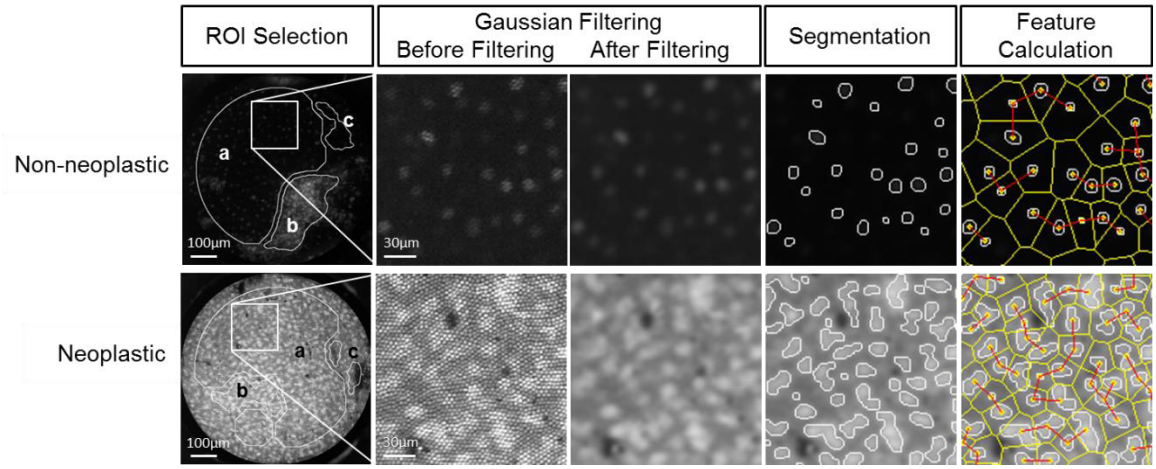

Figure 3. Automated image analysis process. 1) A region of interest (ROI, yellow outline) is selected automatically, excluding image regions which are saturated (red outline) or too dim (purple outline). 2) Fiber pattern is removed using Gaussian filtering. 3) Nuclei are segmented. 4) Quantitative image features are calculated (e.g. nearest internuclear distance).

Images were processed to extract image features of potential use in a classification algorithm. Figure 3 illustrates the image analysis procedure used in this study. While HRME images can reveal important information about epithelial cell morphology and tissue architecture, there are frequently regions of the image which may

be too dim for analysis due to uneven contact of the distal fiber tip with the epithelium, or may be saturated due to the presence of small pieces of debris at the probe tip. Images were first analyzed to exclude such areas of the image and identify an informative region of interest (ROI) for each image. Regions to be excluded were identified by applying a low-pass filter to highlight homogeneous regions of similar intensity and then thresholding the image to reject areas which were too dim or bright for further analysis. Following selection of the informative ROI to be analyzed, Gaussian spatial filtering was applied to remove the background pattern associated with the structure of the fiber bundle used for HRME imaging [47]. Morphologic image processing and thresholding were used to segment nuclei in the HRME image. Morphologic processing (opening and smoothing) was used to compensate for the non-uniform background. Once a threshold was determined by the histogram-based thresholding method, nuclear and cytoplasmic regions were separated by the threshold.

Following nuclear segmentation, the mean, standard deviation, and coefficient of variation of the following features which characterize nuclear morphology were calculated for each image: nuclear size, nuclear-to-cytoplasmic area ratio (N/C ratio), nearest internuclear distance, nuclear eccentricity, nuclear solidity, and major axis of the ellipse best approximating each nucleus.

3.2.4 Automated Image Classification

Features extracted from the HRME images were then used to develop and evaluate an automated classification algorithm to classify whether each site imaged contained neoplastic tissue (HGD, cancer) or was non-neoplastic (normal, inflammation, LGD). The data obtained at The First University Hospital and The Mount Sinai Medical

Center were randomly divided into a training set used to develop and optimize the algorithm, and an independent test set used to estimate algorithm performance. Approximately 1/2 of the images were randomly assigned to the training set and 1/2 to the test set. Randomization was repeated until the proportion of neoplastic sites was approximately the same in the training and validation sets. All images from a single patient were assigned to either the training set or the test set. The data obtained at The Cancer Institute at The Chinese Academy of Medical Sciences were assigned to an independent validation set.

Two-class linear discriminant analysis was used to develop a classification algorithm using data only from the training set; image features were added one at a time until classification performance did not improve further. Histologic diagnosis was considered to be the gold standard. The receiver operating characteristic (ROC) curve for this classifier was plotted using training set data and the optimal threshold was established at the Q-point of the ROC curve. The classification algorithm was then used to classify data in the test and validation sets using this threshold. Sensitivity and specificity were calculated using histologic diagnosis as the gold standard. Finally, ROC curves were plotted for the algorithm applied to the test and validation sets.

3.3 Results

3.3.1 Subject Information – Patients and Sites

A total of 215 subjects were enrolled in the study; images with corresponding pathology results were available from 448 sites in 194 patients. Three reviewers independently agreed on selection of representative images from 303 sites, with 25 of these not passing QC review. In the 145 sites where reviewers disagreed, consensus was

reached on 137 sites, with 40 of these not passing QC review. Images for the remaining 8 sites where consensus could not be reached were not included in further analysis. The remaining data set for further analysis consisted of images from 375 sites in 177 patients. Table 1 shows the histological diagnosis of the measured sites which passed QC review. The data obtained at The First University Hospital and The Mount Sinai Medical Center were randomly separated into training and test sets; 104 sites from 54 patients were assigned to the training set and 104 sites from 45 patients were assigned to the test set. All sites from a single patient were assigned to either the training or test set. The remaining data obtained at The Cancer Institute at The Chinese Academy of Medical Sciences were assigned to an independent validation set which consisted of 167 sites from 78 patients. The composition of the training, test, and validation sets is summarized in Table 2.

Table 1. Histopathologic diagnosis of measured sites.

	Histopathology diagnosis	Sites
Non-neoplastic	Normal	198
	Inflammation	76
	Low-Grade Dysplasia	52
Neoplastic	High-Grade Dysplasia	31
	Cancer	18
	Total	375

Table 2. Training set and validation set composition

	# of patients	# of sites	Histopathologic diagnosis				
			Non-neoplastic			Neoplastic	
			Normal	Inflammation	Low-Grade Dysplasia	High-Grade Dysplasia	Cancer
Training	54	104	70	13	6	8	7
Test	45	104	70	13	6	8	7
Validation	78	167	58	50	40	15	4
Total	177	375	198	76	52	31	18

3.3.2 Quantitative Classification Performance

Quantitative image features were calculated using the automated image analysis. Figure 4 illustrates bar graphs of the mean quantitative image feature values for neoplastic and non-neoplastic tissue in the training set. P values were obtained with the Mann-Whitney U test. The average feature values of non-neoplastic were significantly different from the feature values of neoplastic for all the features.

A two-class linear discriminant algorithm was developed to separate neoplastic and non-neoplastic tissue using each of these six features. The single best performing feature was found to be the mean nuclear area. Figure 5(a) depicts a scatter plot of this feature for each analyzed site in the training set. The decision line associated with the two-class linear discriminant classifier is shown as a straight line on the plot; the

algorithm results in a sensitivity of 93% and a specificity of 92%. Figure 5(b) and 5(c) illustrate this feature for each site in the test and validation sets; the decision line developed using the training set is also shown. Applying the algorithm to data in the test set results in a sensitivity of 87% and a specificity of 97%, and applying it to the data in the validation set results in a sensitivity of 84% and a specificity of 95%. Figure 6 shows the associated ROC curves for this algorithm. The area under the ROC curve is 0.92 in the training set, 0.95 in the test set, and 0.93 in the validation set. The addition of multiple features did not improve algorithm performance.

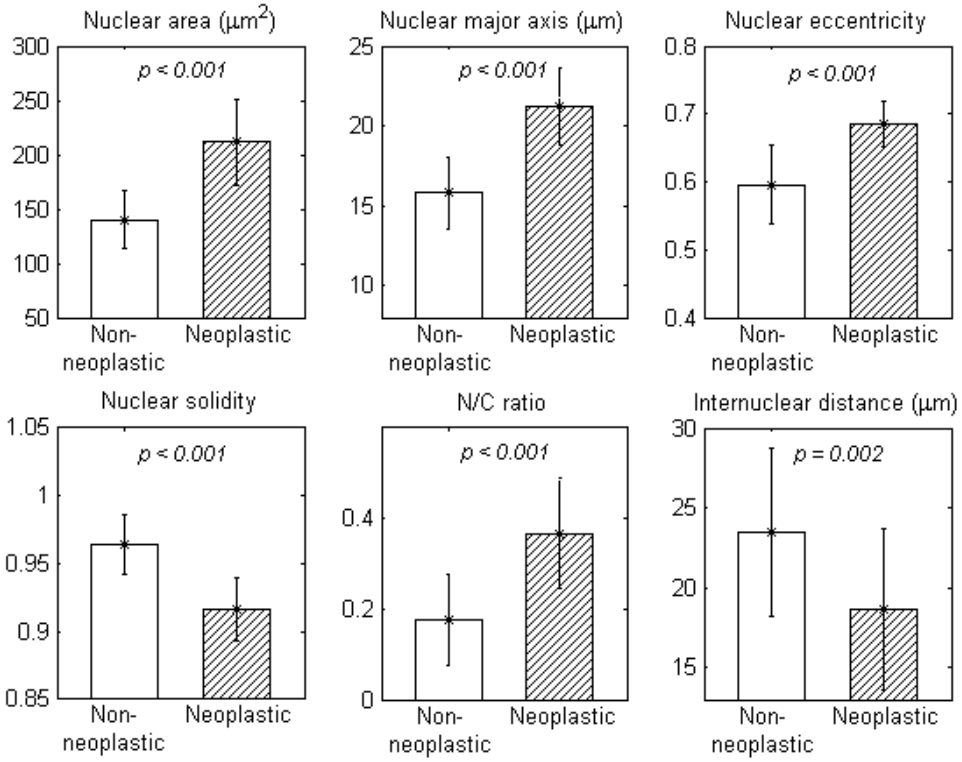

Figure 4. Bar graphs indicating mean values of six quantitative image features (± one std. dev) for non-neoplastic and neoplastic sites in the training set. P-values were obtained using the Mann-Whitney U test.

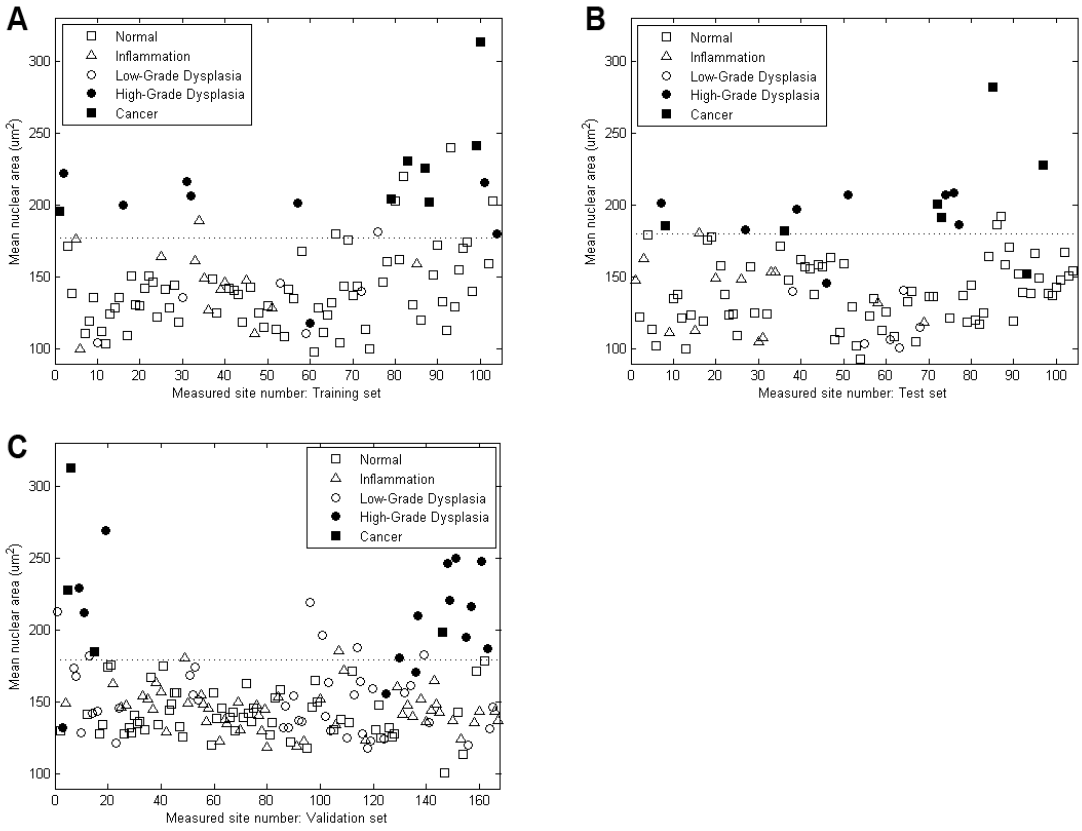

Figure 5. (a) Scatter plot of mean nuclear area for each measured site in the training set. The decision line which classifies sites as neoplastic or non-neoplastic with maximum accuracy is shown. (b) Scatter plot of mean nuclear area for each measured site in the test set. (c) Scatter plot of mean nuclear area for each measured site in the validation set. The decision line to classify sites as neoplastic or not using the training set is shown.

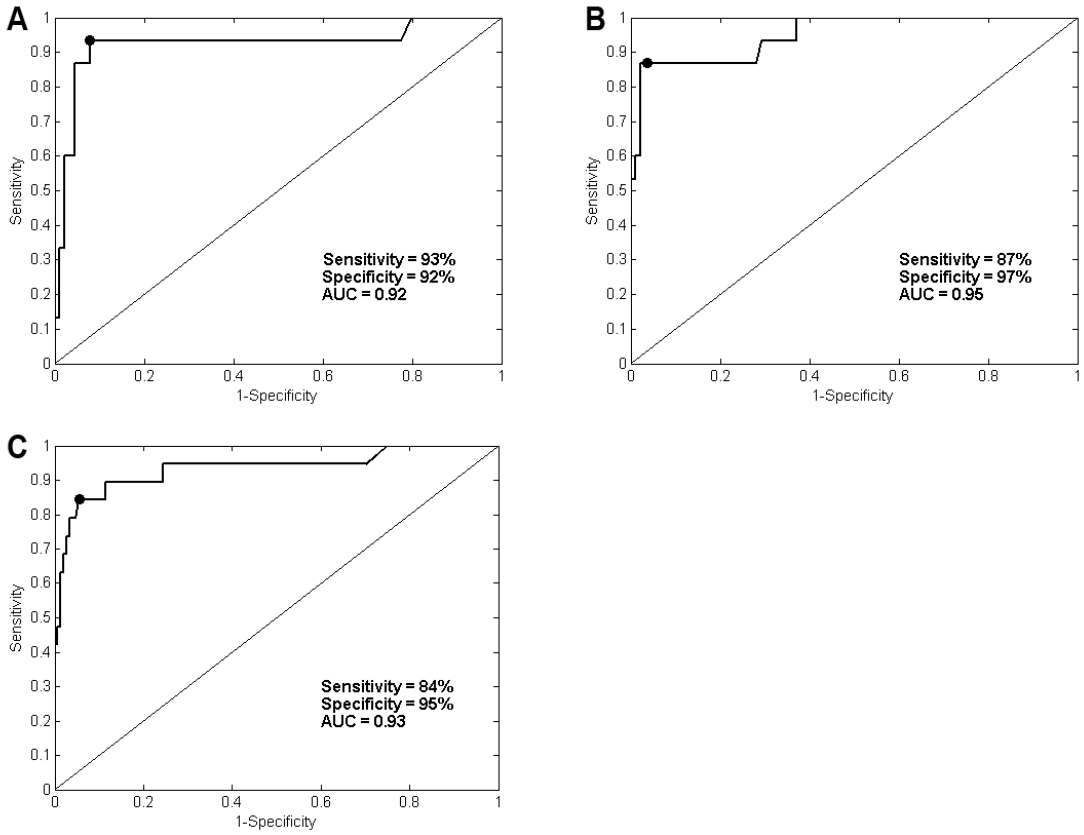

Figure 6. ROC curves for linear discriminant analysis algorithm based on the single feature of mean nuclear area applied to data in (a) the training set, (b) the test set, and (c) the validation. The Q-points correspond to a sensitivity of 93% and a specificity of 92% in the training set (a), 87% and 97% in the test set (b), and 84% and 95% in the validation set (c).

3.4 Discussion

This study assessed the feasibility of automated analysis of HRME images for detection of esophageal squamous neoplasia. Using image analysis tools, we extracted quantitative image features. Data from a training set were used to develop an automated algorithm to discriminate neoplastic from non-neoplastic tissues; data from a test set and an independent validation set were used to evaluate the performance of this algorithm. Mean nuclear area was the image feature with the best performance to discriminate non-neoplastic and neoplastic esophageal squamous epithelium, resulting in a sensitivity of 87% and a specificity of 97% in the test set and 84% and 95% in the validation set compared to the reference standard of histopathology.

Given the limitations of existing screening approaches, the limited availability and high cost of current high resolution platforms, and the uniformly poor prognosis of invasive esophageal carcinoma, there is a great need for more accurate and widely available technologies, particularly in low and middle income countries with high rates of esophageal cancer. A robust, low-cost method of detecting squamous cell neoplasia at an early, resectable stage could markedly improve existing endoscopic screening, surveillance and treatment. While preliminary, the high accuracy and specificity of quantitative analysis of HRME images demonstrated here suggest that this technique could potentially be used to more accurately and selectively target biopsy location. This could reduce the number of biopsies needed for accurate patient diagnosis in low-resource settings where the pathology processing and reading costs are an especially large part of the total cost of patient evaluation and diagnosis. Additionally, the ability to delineate normal from neoplastic mucosa in real-time, if this can be achieved, may

enhance endoscopic margin detection, enabling greater accuracy for complete resection by minimally-invasive endoscopic therapies such as endoscopic mucosal resection, a less costly and less morbid alternative to surgical esophagectomy [48].

The use of automated image analysis potentially reduces the need to train endoscopists to interpret HRME images. It is well known that human interpretation is subject to inter-observer and intra-observer variability, which can limit diagnostic performance [49-51]. Classification based on digital image processing has the potential to reduce the variability of human diagnostic accuracy by providing an objective means to interpret digital images with consistency. This may prove particularly useful in low resource settings where experienced personnel are limited.

The strengths of this study include the fact that it was a multi-center, in vivo study with data from the first two clinical sites randomized to a training set for algorithm development and a separate test set to evaluate the performance of the algorithm relative to the gold standard of histopathology. In addition, performance of the algorithm was assessed in an independent validation set acquired in a different clinical setting than the training and test sets.

A limitation of this study is that image analysis was not performed in real time. Instead, images were analyzed post-hoc, following image acquisition. Furthermore, not all steps of the image analysis procedure were automated. Before the process can be implemented in real-time, it will be necessary to automate frame selection and QC procedures.

Alternatively, the algorithm developed here could be used to enable computer assisted visual image analysis, with automated frame-by-frame analysis supplemented

with visual QC guidance. Figure 7 shows a simple example of how the results of the automated image analysis presented here can be used to guide the development of visual image interpretation guidelines to assist endoscopists in classifying HRME images of the esophagus. Mean nuclear area was found to be the best performing image feature, with samples classified as neoplastic if mean nuclear area exceeds 180 μm^2 (Fig. 5a); this corresponds to a mean nuclear diameter of 15.1 μm assuming circular nuclei. As a simple way to extend this approach to visual image interpretation, we added a row of 15.1 μm diameter dots to the top of each HRME image; in addition, we superimposed a grid with lines spaced 19.4 μm apart to facilitate estimation of nuclear size across the image. Observers are presented an image with the dots and grid superimposed and asked to visually assess whether most nuclei are larger than 15.1 μm in diameter; if yes, then the site is diagnosed as neoplastic. The visual image interpretation guide is now embedded in the HRME imaging software and superimposed on an image window to assist clinicians in identifying neoplastic lesions in real-time at the time of endoscopy.

In summary, the HRME with quantitative image analysis appears to be a promising adjunct that can improve the endoscopic detection of esophageal squamous neoplasia with high accuracy. The lower cost of the technology and the potential for objective image interpretation suggest that it may be feasible for use in low-resource settings. Further analysis is necessary to assess diagnostic accuracy in real time and to determine whether this approach is cost-effective in such settings.

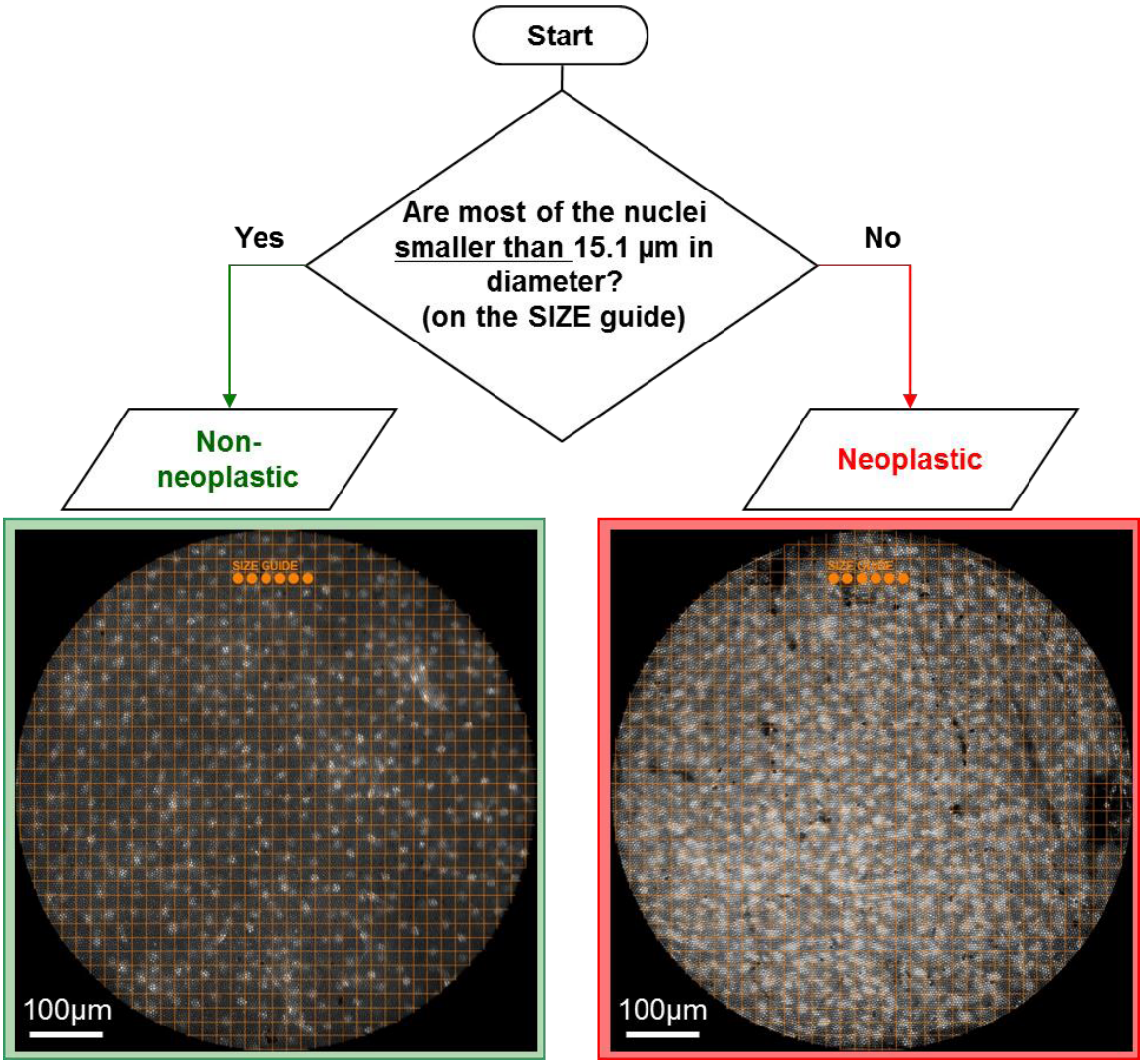

Figure 7. Flow chart illustrating visually-guided image analysis algorithm. A row of 15.1 µm diameter dots was added to the top of each HRME image; in addition, a grid with lines spaced 19.4 µm apart was superimposed to facilitate estimation of nuclear size across the image. If most nuclei appear smaller than 15.1µm in diameter, then the image is classified as non-neoplastic; otherwise it is classified as neoplastic.

Acknowledgements

This work was supported by the National Institute of Health (R01 EB007594 and R21 CA156704).

4. ANALYSIS OF HIGH-RESOLUTION MICROENDOSCOPIC IMAGES FOR QUANTITATIVE DIAGNOSIS OF NEOPLASIA IN PATIENTS WITH BARRETT'S ESOPHAGUS[b]

[b]The contents of this chapter are being prepared for submission.

Abstract:

Background: This study describes an approach for quantitative image analysis of microendoscopic images to identify neoplastic lesions in patients with Barrett's esophagus. This quantitative computer-aided image classification algorithm has the potential to improve diagnostic performance.

Methods: 77 sites in 31 patients were imaged with a fiber optic high-resolution microendoscope (HRME) during a standard endoscopic procedure. Images were analyzed by a fully-automated image processing algorithm, which automatically selected a region of interest (ROI) and calculated quantitative image features. Image features were used to develop an algorithm to identify the presence of neoplasia; results were compared to histopathology diagnosis.

Results: A sequential classification algorithm that utilized image features related to glandular and cellular morphology resulted in a sensitivity of 84% and a specificity of 85%.

Conclusions: This *in vivo* study demonstrates that high-resolution microendoscopic imaging can be used to identify esophageal neoplasia with high accuracy. Automated sequential analysis of microendoscopic images can provide an objective, quantitative framework to assist clinicians in evaluating esophageal lesions from patients with Barrett's esophagus.

4.1 Introduction

Highly prevalent in the US population, Barrett's esophagus (BE) is a major risk factor for the development of esophageal adenocarcinoma (EAC). The incidence rate of EAC is rapidly increasing in the Western World, with an estimated 600% increase in incidence over the last 40 years [1-3, 37]. Moreover, most cases of EAC are diagnosed at a late stage when treatment is challenging, resulting in significant morbidity and a poor 5-year survival rate [52]. Early diagnosis of neoplasia in patients with BE is challenging. Even with routine endoscopic surveillance, it is difficult to identify areas of dysplasia or neoplasia because they may be focal and flat and not visible on standard endoscopy. Endoscopy with random four-quadrant biopsies is the accepted surveillance of BE for identifying the presence of dysplasia. However, four-quadrant biopsies every 2 cm of the Barrett's mucosa can sample only a small fraction of the entire segment of BE ranging from 1 to 20 cm, often resulting in sampling error. Random biopsy protocols have been shown to miss greater than 50% of neoplasia [20, 53]. Improving early detection of BE-associated neoplasia is, therefore, critical to improve survival and quality of life for patients.

Coupled with standard endoscopy, high-resolution optical imaging technologies have the potential to improve diagnostic accuracy for the detection of precancerous and cancerous lesions in patients with BE by allowing real-time imaging with resolution that approaches that of conventional histopatholoty. Confocal microendoscopy can distinguish esophageal neoplasia from benign Barrett's mucosa with high accuracy by providing images of tissue architecture and cellular morphology with subcellular resolution throughout the esophageal epithelium. In several studies, confocal

endomicroscopy combined with high-definition white-light endoscopy (HD-WLE) was shown to significantly improve the ability to detect BE-associated neoplasia [25, 30]. Despite the potential for improving detection of esophageal neoplasia, current confocal platforms are only available to tertiary referral centers due to extremely high-cost ($150,000-$300,000). We recently developed a low-cost (<$5,000) fiber-optic high-resolution microendoscope (HRME), capable of imaging tissue with subcellular resolution comparable to confocal microendoscopy [32]. Muldoon et al. showed the feasibility of the HRME to image various esophageal tissue types, including squamous, BE, and high-grade dysplastic tissue obtained by endoscopic mucosal resection [33]. Pierce et al. demonstrated the ability of the HRME to differentiate high-grade dysplasia from normal squamous mucosa and BE without dysplasia in vivo from a patient with BE [35].

Most studies of high resolution endoscopic imaging rely on subjective visual interpretation. Inter- and intra-observer variability in the assessment of images impair reliable diagnosis. Quantitative analysis offers an objective manner to examine images; the use of computer-aided algorithms may reduce subjectivity among reviewers and enhance reproducibility, resulting in improving diagnostic accuracy. Such algorithms can be coupled with advanced optical imaging techniques with the potential to allow real-time in vivo diagnosis with high accuracy.

In this paper, we report a algorithm to analysis HRME images from patients with BE to distinguish neoplastic from non-neoplastic esophageal mucosa. The sequential classification algorithm was developed based on the sequential rules that expert observers used to classify images based on visual assessment. Performance of the algorithm was

compared with both visual assessment and histopathology, Results demonstrate improved diagnostic performance when using the sequential automated classification algorithm to detect esophageal neoplasia in BE.

4.2 Methods

4.2.1 Patients

Patients with known BE or Barrett's with dysplasia who were scheduled for routine surveillance endoscopy were recruited for this study. Study participants were at least 18 years old and signed a written informed consent and authorization. Persons who were unfit for standard upper endoscopy were ineligible for the study. The study was reviewed and approved by the Institutional Review Boards at Mount Sinai Medical Center and Rice University.

An endoscopist performed a standard upper endoscopic examination. Areas of Barrett's mucosa suspicious for neoplasia during endoscopy were further interrogated with the HRME. Prior to HRME imaging, a topical solution (1-2 ml) of 0.01% proflavine in sterile PBS was applied to the esophageal surface using a standard endoscopic spray catheter. Proflavine, which was used under an Investigational New Drug (IND) application from the Food and Drug Administration (IND 102 217), is a fluorescent contrast agent which stains cell nuclei [44]. Following application of proflavine, the fiber-optic probe of the HRME was inserted through the biopsy channel of the endoscope, and the distal tip was placed in gentle contact with the mucosal surface. Real-time imaging was performed; at each site, video sequences of approximately 3-seconds duration were acquired and then saved to a file. HRME images also were obtained from at least two of four sites selected for random quadrant biopsy. At each site imaged with

the HRME, the fiber probe was used to make a superficial dimple to "mark" the imaged area. Each imaged site was then biopsied and submitted for routine histologic diagnosis. The endoscopist completed a standard of care evaluation by taking the remaining biopsies of the routine four-quadrant biopsy procedure and submitting these for routine histologic diagnosis. All of the specimens were processed and sectioned in a standardized manner. Slides were later reviewed by an expert gastrointestinal pathologist (AP) blinded to the endoscopist's clinical impressions. Diagnosis was performed using standard histologic criteria [45]; based on histologic diagnosis, samples were divided into the following categories: squamous mucosa, gastric cardia, Barrett's metaplasia, low-grade dysplasia (LGD), high-grade dysplasia (HGD), or adenocarcinoma.

4.2.2 Imaging System

The HRME system has been previously described in detail [46]. A bandpass-filtered blue light emitting diode (LED) (FF01-452/25, Semrock, Rochester, NY; M455L2, Thorlabs, Newton, NJ) provides light that passes through a dichroic mirror (485DCLP, Chroma Technology Corp, Bellows Falls, VT) onto a fiber bundle (FIGH-30-850N, Fujikura, Tokyo, Japan) with a 1-mm outer diameter that is placed in contact with the tissue surface to be imaged. The fiber bundle is composed of 30,000 optical fibers with a 4-µm center-to-center spacing and a 720-µm field of view (FOV). Fluorescence emission returns through the fiber bundle and is imaged through the dichroic mirror and a 550-nm bandpass filter (FF03-550/88, Semrock, Rochester, NY). The emission then passes onto the optical sensor of a charge-coupled device (CCD) camera (GRAS-14S5M, Point Grey, Richmond, Canada). The system has a lateral and axial resolution of 4.4 and

20 μm, respectively. A laptop computer controls the system obtains and displays video at a rate of 15 frames per second.

4.2.3 Flowchart for Visual Classification of HRME Images of the Esophagus

HRME images were reviewed for quality control (QC) purposes by two reviewers (RRK, ML). First, one reviewer (ML) identified a single representative image frame from each video sequence. Second, selected images were then reviewed independently for QC by the two reviewers who were blinded to clinical impression and histologic diagnosis. Images were rejected if at least 50% of the FOV was out of focus or showed evidence of motion artifact. Lastly, images that met QC were then reviewed for the selection of a single image with the best image quality per site.

Two reviewers familiar with HRME images of BE from prior studies [35, 47] were asked to classify each image acquired in this study as neoplastic or non-neoplastic. They were blinded to histopathology diagnosis. To assist in the classification, each image was printed on a 3x5 card and reviewers arranged cards according to classification. Reviewers were interviewed following the exercise to understand the sequential rules they used in classification. A flowchart was created to represent the sequential steps followed in visual assessment. The flowchart consisted of decision nodes structured in the form of yes or no questions that led to a specific answer choice. Each question was chosen to describe differences in cell type, cell morphology, and glandular structures, subsequently leading to each category, and then used to extract relevant image features for the following classification analysis.

We also evaluated whether this flowchart could aid endoscopists in making correct visual reads with HRME images of the esophagus. The digital HRME images

were reviewed by three endoscopists with HRME experience. Using the flowchart, reviewers reviewed the entire set of images and recorded an impression for each image as one of the five categories. The categories for squamous mucosa, Barrett's metaplasia, and gastric cardia were considered to be non-neoplastic, while the remaining categories were considered neoplastic. Results of visual image interpretation using the flowchart were calculated for each reviewer.

4.2.4 Automated Image Analysis

Figure 8 illustrates the quantitative image analysis procedure used in this study. At each image, the whole circular FOV was selected for analysis. Low-pass Gaussian filtering was applied to remove the background pattern associated with the structure of the fiber bundle used for HRME imaging [54]. Because the images acquired in this study exhibited different morphologic structures associated with squamous epithelium, intestinal metaplasia, and neoplasia, a variety of image features were explored. First, image intensity was calculated as a feature that could potentially be used to separate squamous tissue from glandular tissue because the fluorescent intensity of glands might be higher than that of squamous-cell nuclei. Second, images were segmented to identify cell nuclei. Morphologic image processing and thresholding were used to segment nuclei in each HRME image. Morphologic processing (opening and smoothing) was used to compensate for the nonuniform background. Once a threshold was chosen by the histogram-based automated thresholding method, nuclear and cytoplasmic regions were separated by the threshold. Following nuclear segmentation, nuclear-to-cytoplasmic area ratio (N/C ratio), mean nuclear size, and mean nearest internuclear distance were calculated for each image.

Lastly, granulometry was used to characterize epithelial thickness and lumen size of glands. Granulometry is a morphologic method to calculate the size distribution of objects in an image without explicitly segmenting each object [18]. HRME images of glandular epithelium exhibit dark lumens with bright epithelial lining. The size distribution of epithelial layer was calculated from each HRME image. Similarly, the size distribution of mucosal lumens was calculated from the inverse of each HRME image. From granulometry, the most frequent size, kurtosis, and skewness of the distribution of the following features were computed for each image: epithelial thickness and mucosal lumen size.

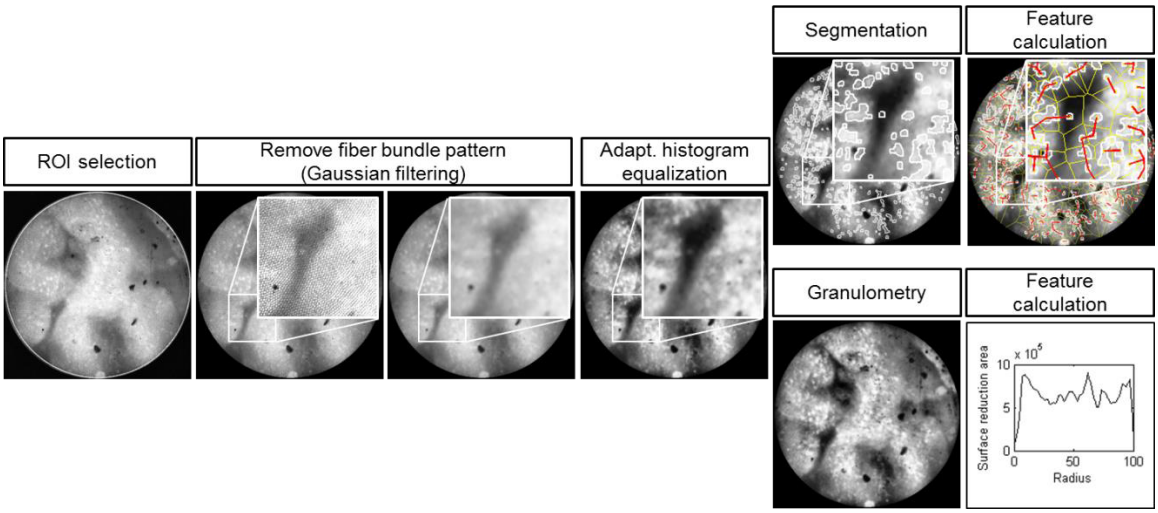

Figure 8. Image analysis process

4.2.5 Automated Image Classification

Features extracted from the HRME images were then used to develop and evaluate an automated sequential classification algorithm to classify whether each imaged site contained neoplastic tissue (HGD or cancer) or was non-neoplastic (normal squamous mucosa, gastric cardia, Barrett's metaplasia, or LGD). Each step of the classification algorithm was identified from the corresponding decision node of the flowchart developed from visual assessment. Two-class linear discriminant analysis was used to develop a classification algorithm at each step; extracted image features were added one at a time until classification performance no longer improved. Sensitivity and specificity were calculated using the sequential classification algorithm and histologic diagnosis as the gold standard.

4.3 Results

4.3.1 Subject Information: Patients and Sites

A total of 36 subjects were enrolled in this study, and 115 sites from 33 patients had corresponding pathology results. Two reviewers (RRK, ML) selected representative images from 87 sites that passed QC review; 28 did not pass QC review. The expert pathologist (AP) reviewed the selected images to see whether they showed different morphology from the histologic diagnosis; 10 sites did not pass QC review. The remaining data set for the subsequent analysis consisted of 77 images from 77 sites in 31 patients. Of these sites, 58 were diagnosed as non-neoplastic and 19 were diagnosed as neoplastic. Table 3 shows the histological diagnosis of the measured sites.

Table 3. Histopathology diagnosis of measured sites.

	Histopathology diagnosis	Site
Non-neoplastic	Squamous mucosa	10
	Gastric cardia	14
	Barrett's metaplasia	25
	Low-grade dysplasia	9
Neoplastic	High-grade dysplasia	9
	Adenocarcinoma	10
	Total	77

4.3.2 Visual Interpretation Using Flowchart

Figure 9 shows the sequential flowchart that was developed for visual classification. Images were categorized into one of five categories. The first question categorized the images based on the presence or absence of glandular tissue. Images that were categorized as not containing glandular tissue were further classified based on the presence of nuclear crowding. Among the images that were categorized as containing glandular tissue, those that contained glandular epithelium with a thin epithelium and large lumen were first separated. The rest of the images were then categorized based on the preservation of regular architecture within the glandular epithelium.

4.3.3 Classification Performance

Quantitative image features were calculated. Relevant image features were selected as described to develop a sequential classification algorithm with optimal

performance. Figure 10 illustrates a classification tree and shows the performance of each node in the tree. At Node 1 of the classification tree, the most frequent epithelial thickness and intensity of the epithelial layer were chosen to classify whether each image contained glandular tissue or not. At Node 2, the N/C ratio was chosen to classify each image into neoplastic or non-neoplastic squamous tissue. The most frequent lumen size and kurtosis of lumen size were chosen at Node 3 to classify each image as cardia or not. The skewness of epithelial thickness was chosen at Node 4 to classify each image into neoplastic or non-neoplastic glandular tissue. Using the sequential classification criteria, 16 of 19 sites were correctly classified as neoplastic, and 49 of 58 sites were correctly classified as non-neoplastic, resulting in a sensitivity of 84% and a specificity of 85%.

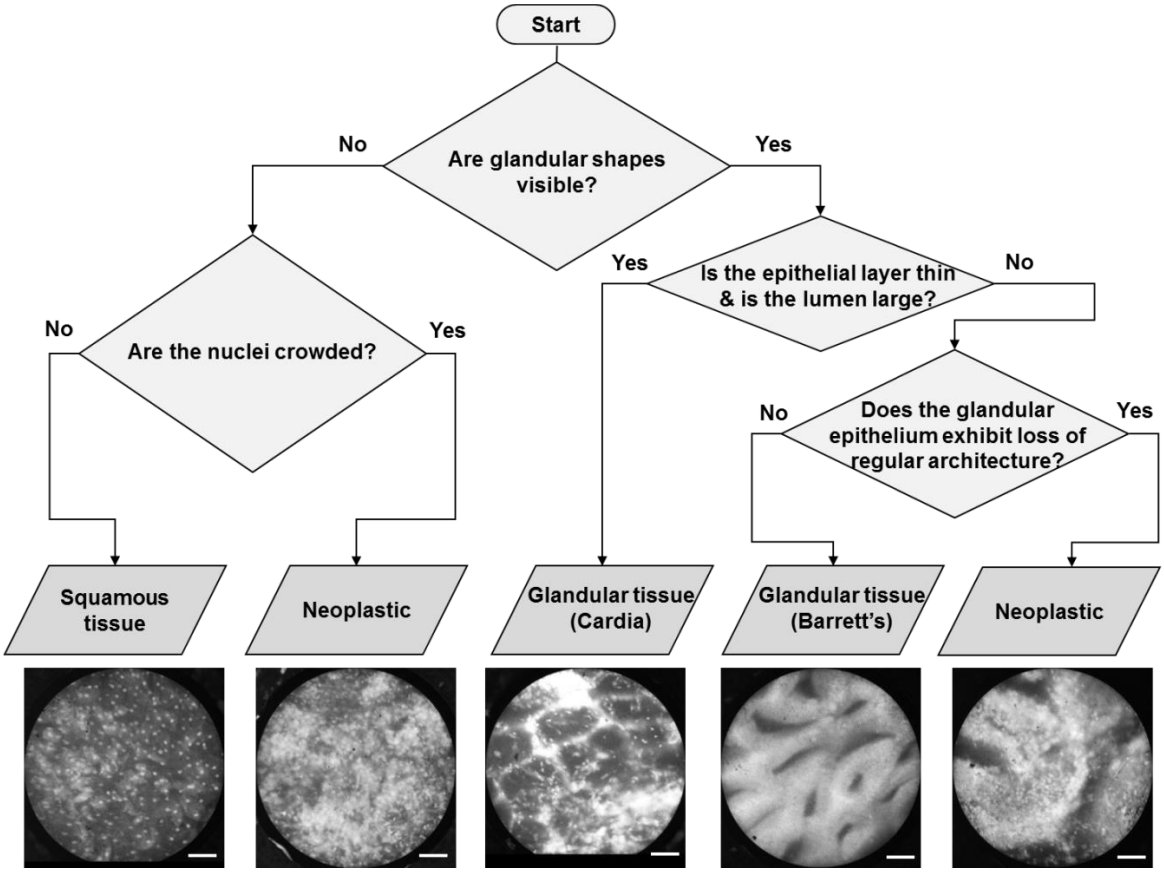

Figure 9. Flowchart for visual classification. Scale bar: 100μm.

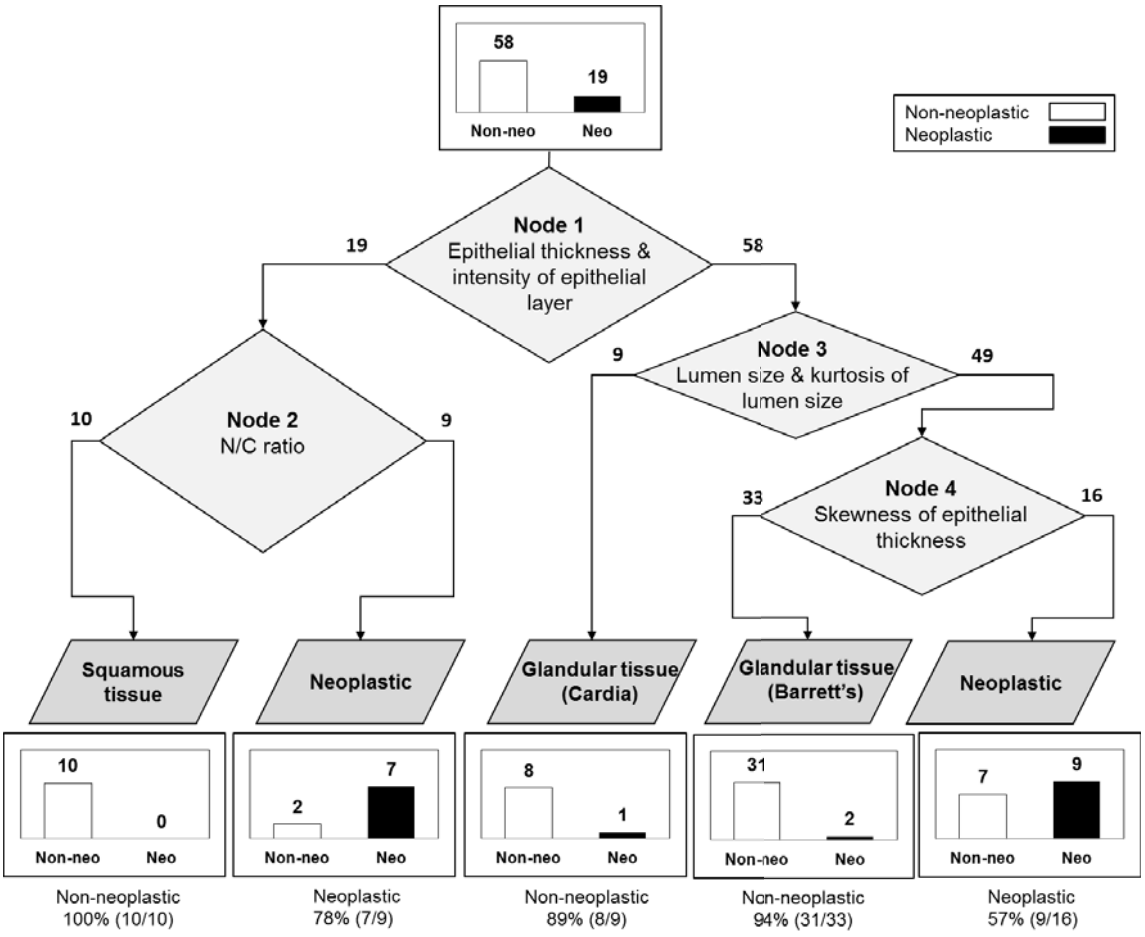

Figure 10. Classification performance

4.4 Discussion

In this study, we demonstrated that HRME imaging could discriminate BE with neoplasia from benign esophageal tissue including normal squamous, BE without dysplasia, and BE with low-grade dysplasia using quantitative image analysis and sequential classification analysis. A classification algorithm was created by sequential analysis of image features within the images, which represented differences in cell type, cell morphology, and glandular structures between non-neoplastic and neoplastic esophageal

tissue. The sequential classification algorithm was able to distinguish between neoplastic and neoplastic tissue with a sensitivity of 84% and a specificity of 85%.

In several studies with confocal endomicroscopy, confocal imaging criteria for BE neoplasia were established and evaluated. Pohl et al. [27] evaluated the use of confocal endomicroscopy in the detection of neoplasia in 296 sites from 38 patients with BE, and achieved a sensitivity of 80% and a specificity of 94.1%, with a corresponding negative predictive value of 98.9%. Similarly, in a study conducted by Gaddam et al. [28], confocal imaging criteria for dysplastic BE were established and evaluated using 50 confocal images, resulting in a sensitivity of 76% and a specificity of 85%. Wallace et al. [51] established confocal imaging criteria in a training set of 20 BE images and tested in an independent validation set of 20 BE images. The study reported a sensitivity of 88% and a specificity of 96%. Although confocal microendoscopy has shown high accuracy for detection of neoplasia, however, inter- and intra-observer variability exist in the interpretation of images obtained with such technique [33, 49, 50]. Rigorous diagnostic criteria using quantitative image analysis can reduce this subjectivity and provide consistent diagnosis with high accuracy. Muldoon et al. developed quantitative image analysis criteria for HRME images from either endoscopically-resected or biopsied tissue to distinguish between neoplastic and non-neoplastic esophageal mucosa [47]. The quantitative analysis using textural features within the images achieved a sensitivity of 87% and a specificity of 85%, while human analysis for the same images achieved average sensitivity and specificity of 87% and 53%, respectively.

The quantitative classification algorithm described in this paper has the potential to improve the accuracy and reproducibility for detection of esophageal neoplasia by

providing an objective means to classify images with consistency. This approach may be of use to clinicians, especially in low-resource settings. Also, it is noted that this sequential classification algorithm used intuitive image features which corresponded well to ones used for visual interpretation of the HRME images, such as epithelial cell morphology and glandular architecture of BE. Alternatively, a framework based on this quantitative classification algorithm can potentially assist endoscopists in the interpretation of HRME images with high accuracy and consistency.

Several other studies have also proposed quantitative analysis of HRME images for diagnosis of neoplasia in patients with oral neoplasia [43, 55] and cervical neoplasia [41, 42]. Analysis used in these studies, however, employed nuclear segmentation to distinguish differences in cell morphology of neoplastic tissue. It is difficult to extend this approach to analysis of images from patients with neoplasia in the glandular epithelium, which exhibits differences in not only nuclear morphology but also glandular architecture [35, 36]. The quantitative classification algorithm presented here could be applied to any analysis of HRME images of the glandular epithelium where a variety of tissue types exist. Furthermore, confocal imaging of the gastrointestinal epithelium could be advantaged by this quantitative classification analysis.

A limitation of this study is the small field of view (720 μm in diameter) of the HRME. Often, dysplastic changes in BE occur focally; the HRME may not image the area of dysplasia correctly. This might be, also, because the positioning of the HRME probe during endoscopy is difficult at BE. Considerable training on the endoscopic positioning of the HRME probe will be necessarily required for better diagnostic yield.

The use of the HRME and quantitative diagnostic algorithm presented here could potentially impact the application of high-resolution microendoscopy as a useful tool in low-resource settings by providing a cost-effective and reliable method for detecting esophageal neoplastic lesions during endoscopy. Further evaluation of this classification algorithm in real-time will be necessary in clinical practice, particularly in resource-poor settings.

5. A FIBER-OPTIC FLUORESCENCE MICROSCOPE USING A CONSUMER-GRADE DIGITAL CAMERA FOR IN VIVO CELLULAR IMAGING[c]

[c]The contents of this chapter have been published in the following journal article: Shin D, Pierce MC, Gillenwater AM, Williams MD, Richards-Kortum RR. A fiber-optic fluorescence microscope using a consumer-grade digital camera for in vivo cellular imaging. *PLoS One*. 2010;5(6):e11218.

Abstract: Early detection is an essential component of cancer management. Unfortunately, visual examination can often be unreliable, and many settings lack the financial capital and infrastructure to operate PET, CT, and MRI systems. Moreover, the infrastructure and expense associated with surgical biopsy and microscopy are a challenge to establishing cancer screening/early detection programs in low-resource settings. Improvements in performance and declining costs have led to the availability of optoelectronic components, which can be used to develop low-cost diagnostic imaging devices for use at the point-of-care. Here, we demonstrate a fiber-optic fluorescence microscope using a consumer-grade camera for in vivo cellular imaging. The fiber-optic fluorescence microscope includes an LED light, an objective lens, a fiber-optic bundle, and a consumer-grade digital camera. The system was used to image an oral cancer cell line labeled with 0.01% proflavine. A human tissue specimen was imaged following surgical resection, enabling dysplastic and cancerous regions to be evaluated. The oral mucosa of a healthy human subject was imaged in vivo, following topical application of 0.01% proflavine. The fiber-optic microscope resolved individual nuclei in all specimens and tissues imaged. This capability allowed qualitative and quantitative differences between normal and precancerous or cancerous tissues to be identified. The optical efficiency of the system permitted imaging of

the human oral mucosa in real time. Our results indicate this device as a useful tool to assist in the identification of early neoplastic changes in epithelial tissues. This portable, inexpensive unit may be particularly appropriate for use at the point-of-care in low-resource settings.

9.1 Introduction

Point-of-care diagnostic devices should be small, inexpensive, and portable, yet accurate, robust, and simple to use. Optical imaging techniques can play a crucial role in the realization of such technologies, by providing real-time, high-resolution diagnostic information in non- or minimally-invasive fashion. In addition, flexible, miniature fiber-optic components have made it possible to access tissue at confined sites within the body, enabling cellular level imaging to be performed in tandem with standard wide-field methods, such as endoscopy. These capabilities are currently being investigated for potential roles in clinical diagnostics, screening, and surgical guidance [32, 33, 56-62], but for translation of the technology to the point-of-care setting to become realistic, issues of cost, complexity, size, and performance must be addressed.

Rapid improvements in the technical specifications and cost efficiency of consumer-grade electronics have brought high-performance imaging devices to the general market. Low-cost, high-quality digital cameras are now available with over 20 megapixel image sensors (for example the Canon EOS-1Ds mark III); Sony-Ericsson's Satio model cellular phone has 12.1 megapixels. SLR (Single Lens Reflex) digital cameras are relatively inexpensive in comparison to the scientific-grade CCD cameras which are used in many biological imaging applications [63-65]. Most of these cameras are powered by a rechargeable battery pack and include a built-in LCD screen for real-

time visualization. These features can support the design of imaging systems that are low-cost, battery-powered and completely portable. Indeed, studies have employed digital SLR cameras for macroscopic image acquisition of biological tissues [66-69], and also for recording images of cells and tissue sections on conventional and portable microscopes [70].

Microscopic scale imaging in vivo has thus far been developed through techniques such as confocal microscopy, using flexible, narrow fiber-optic probes to access superficial tissues such as the skin, or hollow cavities such as the oral cavity, bronchus, cervix or GI tract [32, 33, 56-59]. While these systems have demonstrated the capacity to provide high-quality images, the requirements of laser sources, scanning mechanism(s), and high-speed digitizing hardware all contribute to a price tag well out of the range of many healthcare settings. Our group [32], [33], and others [56], [60], [62] have recently demonstrated sub-cellular resolution wide-field imaging through a fiber-optic bundle. By using a wide-field epi-fluorescence arrangement instead of point-scanning, the system complexity and cost are greatly reduced. When used with bright, fluorescent contrast agents, sub-cellular morphology can be viewed in real-time, by simply placing the distal end of the bundle onto the tissue site to be imaged.

Here we present a high-resolution fiber-optic fluorescence imaging system using a consumer-based digital camera to visualize sub-cellular features in living tissue. We demonstrate the capabilities of the system through a series of experimental studies. First, we carried out imaging of a cultured cell model of an oral cancer cell line labeled with fluorescent dye. Next, we performed imaging of a surgically-resected human tissue specimen, including dysplastic and cancerous regions. Finally, a healthy human subject

was imaged in vivo. These studies demonstrate the capability of the system to obtain images with sub-cellular resolution, non-invasively, and in real-time. We propose that this portable, inexpensive diagnostic imaging device may be useful as an efficient diagnostic tool at the point-of-care for populations in remote or rural communities in the U.S. as well as in developing countries.

9.2 Materials and methods

Fiber-optic microendoscope system using a consumer-grade digital camera

The main components of the system include an LED light source, a microscope objective lens, a fiber bundle and a digital camera as shown in Figure 11. The LED light source emits an optical spectrum centered at 455 nm with 20 nm spectral bandwidth (full-width half-maximum). Following a 450 nm bandpass filter (Thorlabs, FB450-40) and a 475 nm dichroic mirror (Chroma, 475DCXRU), excitation light illuminates the proximal end of a 1 mm diameter coherent fiber-optic bundle (Sumitomo, IGN-08/30). The distal end of the bundle is placed in direct contact with the sample to collect fluorescence emission, which then returns through the bundle and is imaged on to the optical sensor of the digital camera by a 20×/0.40 NA infinity-corrected objective lens (Olympus) and a 150 mm tube lens. For proflavine (Sigma, P2580) used as a contrast agent, a 500 nm long-pass filter (Thorlabs, FEL0500) was placed in infinity space. The objective and the tube lens combination form a magnified image of the bundle on the sensor of the camera, which is visualized on the LCD screen of the camera in real-time. The camera also allows connection to a laptop or other monitor screen through USB or composite video cables. The entire system weighs 3.5 pounds, is powered by a rechargeable battery, and operates for about one hour on a single charge. The overall cost of the system is about $2,000

including the $400 digital SLR camera body. The SLR camera specifications are summarized and compared with those of the scientific-grade CCD camera used by Muldoon et al. [32] in Table 1.

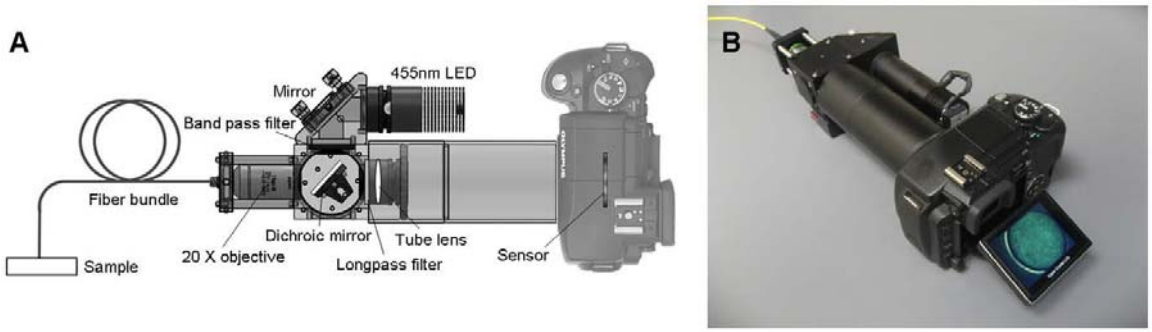

Figure 11. High-resolution fiber-optic microendoscope. (A) Schematic diagram of the system. (B) Photograph of the system.

Table 4. Experimental parameters of systems.

	Olympus E-330	Muldoon *et al.* [32]
Array size (mm)	17.3 x 13.0	10.2 x 8.3
Pixel size (μm)	5.6 x 5.6	6.45 x 6.45
Number of pixels	3136 x 2352	1392 x 1040
Relay magnification	19.5 x	8.3 x
Pixels per fiber at CCD	7.68	2.85
CCD dynamic range	43 dB	67 dB

Cell culture and labeling

Proflavine is a fluorescent stain which labels cell nuclei by intercalating between DNA base pairs [44]. Absorption and emission maxima are at approximately 445 and 510 nm, respectively. 1483 oral cancer cells derived from a human oropharyngeal squamous carcinoma were stained with proflavine (0.01% w/v in PBS, Sigma P2508) and then suspended in collagen for imaging.

Surgical specimen acquisition and imaging

Through a study protocol approved by both Rice University and the University of Texas M.D. Anderson Cancer Center Institutional Review Boards, and following written informed consent by the patient, a surgical specimen was obtained immediately after resection. Following topical application of proflavine (0.01% w/v in PBS, Sigma P2508) to the mucosal surface, images were obtained with the fiber-optic microendoscope. The specimen was sent for routine histopathology; H&E sections were prepared, including from the sites imaged with the fiber-optic microendoscope. Proflavine staining does not affect subsequent H&E staining for histologic analysis.

Human subject imaging

The oral mucosa of a healthy human subject who had given written informed consent was imaged in vivo using the fiber-optic microendoscope in accordance with a protocol approved by the Rice University Institutional Review Board. The participant in this manuscript has given written informed consent (as outlined in the PLoS consent form) to publication of his/her case details. Proflavine was obtained in powder form from Sigma (P2508) and prepared in solution for imaging by dissolving in PBS (0.01% w/v) and sterile filtered prior to use. Proflavine was topically applied to a small area of the mucosal surface. After only a few seconds of application, the distal tip of the fiber-optic bundle was placed in direct contact. Real-time observation of sub-cellular detail at the imaged site was possible via the camera's LCD screen (Figure 11 (B)). Images recorded for additional analysis were stored on the camera's removable memory card.

9.3 Results

System characterization

Spatial resolution was measured by imaging a Ronchi grating and calculating the distance across the edge over which intensity ranged from 10% to 90% of the maximal value. The 10–90% distance was found to be 5.0 μm. The spatial resolution is currently limited by under-sampling due to the 4 μm core-core spacing between individual elements in the coherent fiber-optic bundle; Figure 12 shows that the system can resolve the G6 E6 lines of a USAF resolution target (line width = 4.4 μm). The size of the individual fibers is 2.2 μm and there are approximately 30,000 fibers in the bundle. We assessed the depth-of-field of the system by measuring images of a USAF resolution target as the distance between the fiber tip and the surface of the target was increased. Results show that the depth of focus is approximately 20 μm, based on the distance at which the contrast between the G6 E6 lines was reduced to 26% of its maximal value (Rayleigh). The imaged field-of-view corresponds to the physical area of the fiber bundle face, which is 800 μm in diameter. In the system presented here, the fiber-bundle image slightly overfills the sensor of the camera, resulting in an achieved field-of-view of 660 μm. The optical power delivered to the distal tip of the fiber bundle was measured to be 0.5 mW, corresponding to an average irradiance level of 100 mW/cm^2.

1483 oral cancer cell imaging

Images of 1483 oral cancer cells labeled with proflavine obtained using the fiber-optic microendoscope are shown in Figure 13. Owing to labeling with proflavine, cell nuclei appear bright in the image. Images acquired with the SLR-based system (Figure 13 (A)) were compared to those obtained with a scientific CCD-based microendoscope (Figure 3

(B)) [32], with both images acquired at the same sample site, under identical illumination conditions. The power measured from the fiber bundle was 0.5 mW for each image. We summarized the experimental parameters of these two microendoscope systems in Table 1. The SLR-based image (Figure 13 (A)) was taken with a 1 second integration time at the lowest ISO setting (ISO 100). The CCD-based image (Figure 13 (B)) was taken with a 1 second integration time at 0 dB gain. Each image was separated into labeled (signal) and unlabeled (background) regions in software by setting an intensity-based threshold. The average grayscale intensity of the pixels in the labeled regions in the SLR-based image was 80.4. The corresponding average intensity in the CCD-based image was 138.9. The signal-to-background ratio measured in the SLR-based image was 2.88 and 3.67 in the CCD-based image. The average pixel intensity of the black level measured in the SLR-based system was 2.3 and 5.6 in the CCD-based system; it is not possible to manually adjust the offset level in either system.

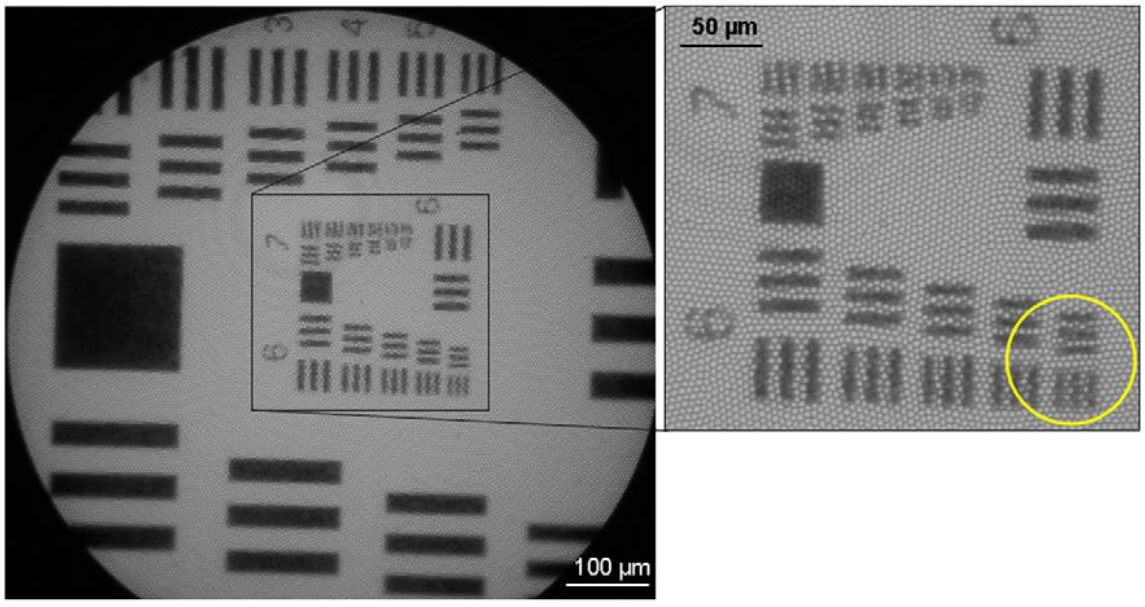

Figure 12. USAF resolution target image.

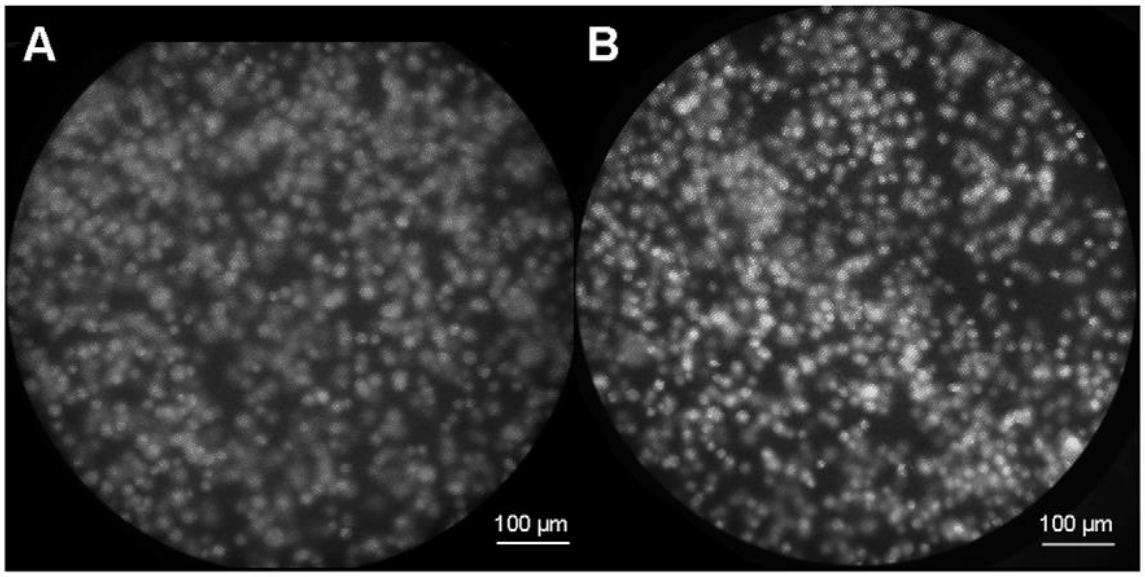

Figure 13. 1483 oral cancer cell images using proflavine as a contrast agent to visualize cell nuclei. (A) Image acquired with the SLR-based microendoscope. (B) Image acquired with the scientific CCD-based microendoscope.

Ex vivo human specimen imaging

Images obtained from a surgically resected oral tissue specimen containing an oral squamous carcinoma located in the right posterior floor of mouth are shown in Figure 4. Each image was acquired with a 0.25 s integration time and ISO 400. The distal tip of the fiber-optic bundle was placed in direct contact with the specimen at regions appearing clinically normal and abnormal, as shown in the accompanying photographs. In microendoscope images, regularly-distributed nuclei appear as discrete, bright dots throughout the field-of-view at the clinically-normal region (Figure 14 (A)). Near the tumor margin, the nuclear density exhibited the characteristic increase associated with neoplastic progression (Figure 14 (B)). The image obtained at the region containing the tumor demonstrates the characteristic features associated with cancer such as dense and disorganized nuclei (Figure 14 (C)). From the microendoscope images, we quantified the

nuclear-to-cytoplasmic (N/C) area ratio, which is an important parameter used in the

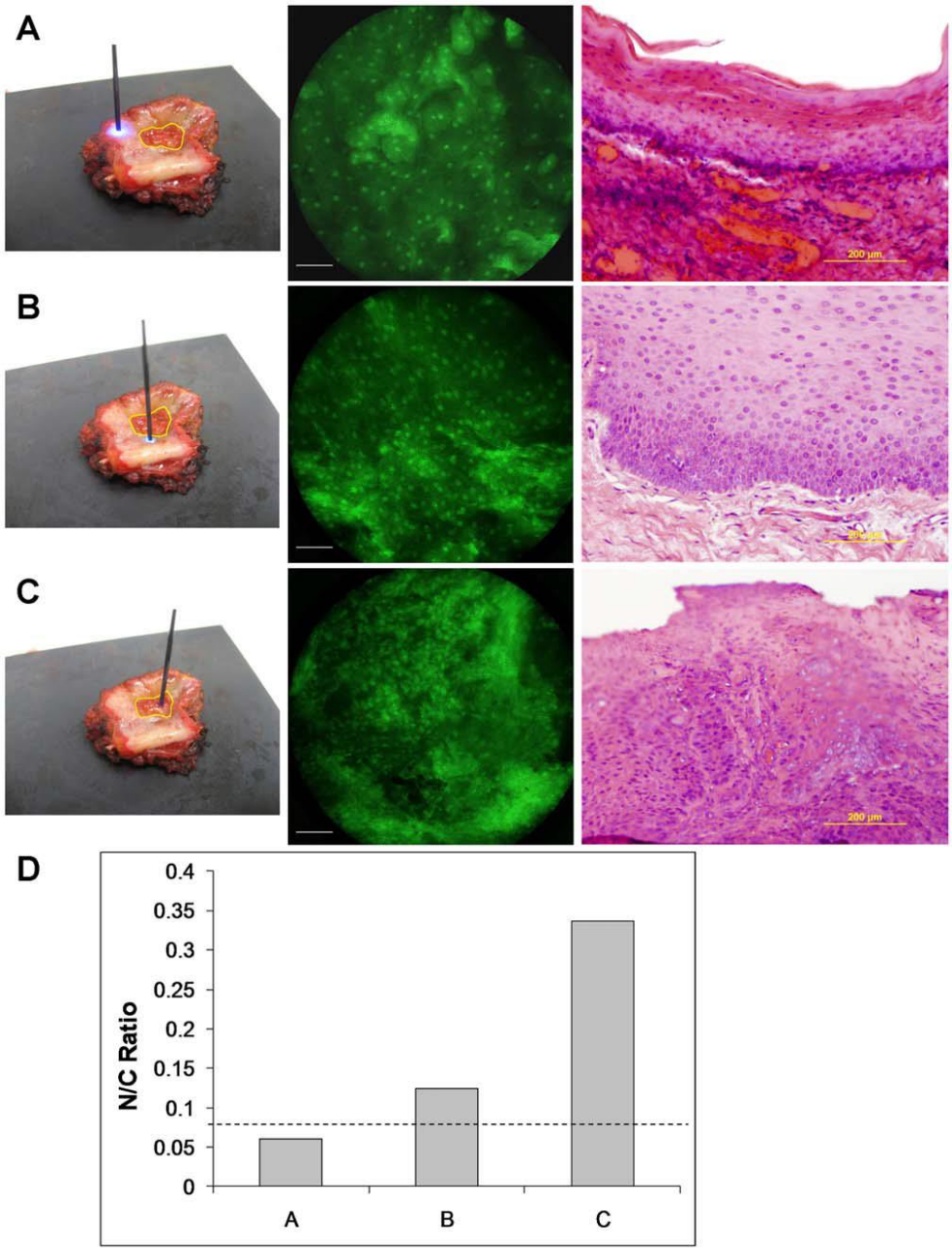

Figure 14. Ex vivo human specimen imaging. (A) Normal epithelium. Left; photograph of fiber bundle probe in contact with resected tissue at clinically-normal region. Yellow border represents margin of clinically-abnormal region identified by the surgeon. Center; image taken with fiber-optic microendoscope. Scale bar represents 100mm. Light; corresponding histopathology section demonstrating normal epithelium. (B) Mild dysplasia. Probe placed at region near to margin of tumor (left). Corresponding histopathology section demonstrates mild dysplasia. (C) Cancer. Probe placed at clinically-abnormal region. Corresponding histopathology section demonstrates squamous carcinoma. (D) Calculated N/C ratio of images in (A, B and C). The dashed line represents an N/C ratio of 0.08.

histological diagnosis of cancer. Using morphological image processing methods, nuclei were segmented based on a pixel intensity threshold, defining nuclear and cytoplasmic regions. N/C ratio was then calculated from the number of pixels in each region. The N/C ratio for the images shown in Figure 14 (A, B and C) was calculated to be 0.06, 0.12 and 0.34 respectively (Figure 14 (D)), which may be compared to the threshold value of 0.08, established by Collier et al. as a means of discriminating between normal (lower N/C ratio) and cervical intraepithelial neoplasia (higher N/C ratio) [71]. The corresponding histology in Figure 14 (A) demonstrates normal epithelium, while Figure 14 (B) indicates mild dysplasia and Figure 14 (C) indicates squamous carcinoma.

In vivo human subject imaging

Figure 15 demonstrates the characteristics of normal human oral mucosa imaged in vivo, including bright and regularly-distributed nuclei labeled by proflavine. The calculated N/C ratio for this image is 0.05. The image presented in Figure 5 (B) is a single frame acquired during real-time imaging at 4 frames per second.

9.4 Discussion

Several studies have previously investigated the use of compact digital cameras or cell phone cameras for biomedical imaging applications. Consumer-grade cameras have been used for wide-field fluorescence imaging [66-69], pathology analysis [70], and the on-board cameras of cell phones [72-76] and PDAs [77] have been used in clinical applications. Here we demonstrated a portable high-resolution fiber-optic fluorescence imaging system for in vivo cellular imaging. The system leverages the increasing level of imaging performance which has become accessible at relatively low-cost through the consumer electronics market. The use of a digital camera has several practical benefits;

the system incorporates an LCD screen for real-time image visualization, thus eliminating the requirement for additional hardware for image processing and display. While digital camera displays have increased in size and resolution in recent years, many cameras can also transmit images to a larger external monitor via USB or composite video cables. Digital camera units are also battery-powered, enabling a completely portable imaging system to be assembled.

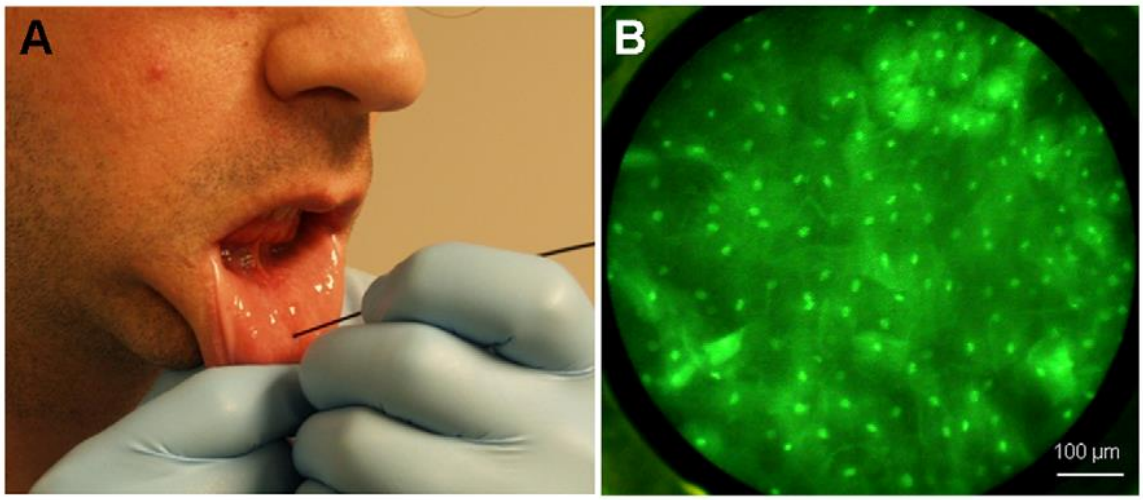

Figure 15. In vivo image of human volunteer.

The images obtained here were obtained using the contrast agent, proflavine. Proflavine is inexpensive, has a long history of safe clinical use, and fluorescence images of epithelial cells can be obtained with high contrast between the cytoplasm and nucleus within seconds after topical application. Proflavine is the principal component of acriflavine and has been used for fluorescence imaging in the European, Asian, and Australian gastrointestinal literature without any adverse effects noted [78]. Moreover, proflavine has been used clinically as an antibacterial agent for decades. In neonatal care,

Triple dye, a combination of brilliant green, proflavine hemisulfate, and gentian violet is routinely used as a topical antibacterial agent on the umbilical stump of newborn babies [79], with a recent review of the practice categorizing toxicity as rare [80]. The concentrations of proflavine solution required for successful imaging (0.01–0.05%) [78] are substantially lower than that of the proflavine component in commercial triple dye, 0.11% (w/v) (VistaPharm, Kerr Triple Dye). The quantity of solution required for diagnostic imaging is approximately the same as that used in neonatal care (0.65 ml per single-use swab). The additional exposure to light which will occur during imaging can also be compared to that received by newborn babies undergoing phototherapy for jaundice. The high-resolution fiber-optic microendoscope proposed for use here delivers 0.5 mW of 455 nm light to the tissue through a 0.8 mm diameter fiber-optic bundle, corresponding to an irradiance level of 100 mW/cm^2. The American Academy of Pediatrics defines intensive phototherapy as a spectral irradiance of at least 30 W/cm^2 per nanometer over the 430–490 nm spectral band, equivalent to a total irradiance of 1.8 mW/cm^2 [81]. Although the irradiance level is over 50-times higher with the fiber microendoscope system, a typical imaging session of 30 minutes (including imaging for routine care) is approximately 50-times shorter than a typical 24 hour (1440 minutes) phototherapy incubation, leading to an equivalent light dose in each scenario. Proflavine has also been safely used in previous clinical studies evaluating its effect as a photosensitizing agent for the treatment of genital herpes simplex virus [82]. Precancers of the epithelium are associated with a variety of morphological changes including increased nuclear size, pleomorphism, nuclear hyperchromasia and increased N/C ratio [83]. Clinical pathologists currently assess these features qualitatively, by examining

stained sections at low and high power magnification. Recently, a number of studies have shown that quantitative analysis of digital images of stained histologic sections can aid in the identification of precancers [84]. In quantitative pathology, measurements of morphological and architectural features are used to make the diagnosis. In both cases, the morphologic information is acquired from stained tissue sections taken from biopsies, which are invasive, expensive, and painful and limit the area at risk which can be examined. In vivo microscopy provides an alternative approach to assess these morphologic changes in vivo. For example, nuclear morphometry acquired from two dimensional confocal images of the cervical epithelium can be used to distinguish normal epithelium from high grade dysplasia in the cervix [85].

As high resolution in vivo imaging systems such as the one presented here achieve more widespread clinical application, there is a growing need for image atlases to help clinicians and pathologists interpret these types of images. Such tools are beginning to be developed. For example, the Digital Atlas of Video Endoscopy (DAVE) is an endoscopic education tool containing both high-resolution images and videos of different gastrointestinal procedures and disorders. Developed in collaboration with the American Society of Gastrointestinal Endoscopy (ASGE), the largest endoscopic society worldwide, the DAVE project serves as an initial and free platform for dissemination to the public [86].

Modern digital cameras are also capable of on-board image processing. Pathologically relevant morphologic markers including nuclear size, distribution, and N/C ratio could potentially be extracted from images using relatively straightforward analysis algorithms. This information could be used to assist non-expert medical

personnel in reaching a diagnosis, by providing quantitative evaluation of images in real-time. Alternatively, the same information could be used to guide the healthcare provider in biopsy site selection, by locating those sites with the highest suspicion for disease. The flash memory cards used for image storage are also widely compatible with cell phone and PDA hardware, enabling image transmission to remote experts in situations where further diagnostic interpretation is necessary.

A potential clinical application area for this type of cost-effective, compact imaging system may emerge in early cancer screening, particularly in developing countries. In the foreseeable future, the burden of cancer will continue to shift onto the populations of these regions, where early detection through screening programs offers the only opportunity to implement affordable treatment. Real-time diagnosis at the time of a clinical visit is also critical in reducing loss of patients to follow-up, and enables "see-and-treat" programs to be carried out. Several epithelial cancers such as those of the uterine cervix, oral cavity, and esophagus are significant contributors to mortality and morbidity in developing countries, and a high-resolution in vivo imaging system such as the one presented here could have significant impact on the management of these cancers.

In conclusion, we believe that recent advances in imaging performance coupled with declining costs will enable further development of clinically viable diagnostic imaging systems based upon consumer-grade electronics. Such instruments may find use in developing countries with limited technical and financial resources, or in industrialized nations with inefficient, overpriced healthcare systems.

Acknowledgements

We thank Vivian Mack (Rice University) for providing cell samples and cell culture.

6. CONCLUSION

In summary, several clinical studies were performed to evaluate the effectiveness of quantitative classification algorithms for HRME images to distinguish between esophageal neoplastic and non-neoplastic tissue. A study of HRME in 177 patients with ESCC resulted in a sensitivity and specificity of 93% and 92%, respectively, in the training set, 87% and 97%, respectively, in the test set, and 84% and 95%, respectively, in an independent validation set using mean nuclear area as the basis for classification. Another study in 31 patients with esophageal BE resulted in a sensitivity of 84% and a specificity of 85% using a sequential quantitative classification algorithm. Given the diagnostic performances of HRME and quantitative classification algorithms in these studies, there was a need for a more portable and cost-effective system with comparable performance to the existing HRME. A portable fiber-optic microendoscope using a consumer-grade digital camera was developed, and a series of biomedical experimental studies were performed to evaluate the capability and portability of the device.

The results reported here confirm that HRME with a classification algorithm can be a useful tool for screening and surveillance of esophageal neoplasia. Automated analysis of microendoscopic images can potentially provide an objective quantitative means to assist clinicians in evaluating esophageal lesions. Combined with the portable fiber-optic microendoscope based on a consumer-grade camera, the quantitative classification algorithm can be used, particularly in low-resource settings. Challenges that remain for the use of HRME with the classification algorithm in a clinical setting include implementing a fully-automated image analysis of the entire process and evaluating its diagnostic performance in vivo. To address these challenges, it will be necessary to

automate the entire process by implementing automated frame selection and QC procedures and to embed the quantitative classification algorithm in the HRME imaging software for real-time diagnosis. Alternatively, a visual interpretation guide was created based on the quantities found in the algorithm to assist clinicians in detecting esophageal neoplasia in real-time during endoscopy. Another challenge includes the proper use of cost-effective consumer-grade electronics in the imaging system. Given the rapid improvements in these electronics, this challenge can be effectively addressed using appropriate technology; for example, the camera of a cellular phone can be used as a cost-effective imaging system, which can then be coupled with the quantitative analysis algorithm based on open-source principles.

High-resolution imaging combined with quantitative analysis may enhance the performance of optical imaging for real-time objective detection of esophageal neoplastic lesions during endoscopy. While this computer-aided diagnostic imaging system has yielded interesting results, it has not yet been evaluated in low-resource settings. As such, future studies will need to evaluate the cost-effectiveness of this technique in such settings.

7. REFERENCES

1. Ferlay J, Shin HR, Bray F, Forman D, Mathers C, Parkin DM. Estimates of worldwide burden of cancer in 2008: GLOBOCAN 2008, *Int J Cancer*. 2010;127(12):2893–2917.
2. Jemal A, Bray F, Center MM, Ferlay J, Ward E, Forman D. Global Cancer Statistics. *CA Cancer J Clin*. 2011;61(2):69-90.
3. Pohl H, Welch HG. The role of overdiagnosis and reclassification in the marked increase of esophageal adenocarcinoma incidence. *J Natl Cancer Inst*. 2005;97(2):142-6.
4. Guo P, Li K. Trends in esophageal cancer mortality in China during 1987-2009: age, period and birth cohort analyzes. *Cancer Epidemiol*. 2012;36(2):99-105.
5. Hayat MJ, Howlader N, Reichman ME, Edwards BK. Cancer statistics, trends, and multiple primary care analyses from the Surveillance, Epidemiology, and End Results (SEER) Program. *Oncologist*. 2007;12(1):20-37.
6. Sihvo EI, Luostarinen ME, Salo JA. Fate of patients with adenocarcinoma of the esophagus and the esophagogastric junction: a population-based analysis. *Am J Gastroenterol*. 2004;99(3):419-24.
7. Portale G, Hagen JA, Peters JH, et al. Modern 5-year survival of resectable esophageal adenocarcinoma: single institution experience with 263 patients. *J Am Coll Surg*. 2006;202(4):588-96; discussion 596-8.
8. Wang GQ, Abnet CC, Shen Q, et al. Histological precursors of oesophageal squamous cell carcinoma: results from a 13 year prospective follow up study in a high risk population. *Gut*. 2005;54(2):187-192.

9. Kelloff GJ, Sigman CC. Assessing intraepithelial neoplasia and drug safety in cancer-preventive drug development. *Nat Rev Cancer*. 2007;7(7):508-518.
10. Mueller J, Werner M, Stolte M. Barrett's esophagus: histopathologic definitions and diagnostic criteria. *World J Surg*. 2004;28(2):148-54.
11. De Palma GD. Management strategies of Barrett's esophagus. *World J Gastroenterol*. 2012;18(43):6216-25.
12. Reddymasu SC, Sharma P. Advances in endoscopic imaging of the esophagus. *Gastroenterol Clin North Am*. 2008;37 (4):763-74.
13. Dawsey SM, Fleischer DE, Wang GQ, et al. Mucosal iodine staining improves endoscopic visualization of squamous dysplasia and squamous cell carcinoma in Linxian, China. *Cancer*. 1998;83:220-231.
14. Hashimoto CL, Iriya ER, Baba, et al. Lugol's dye spray chromoendoscopy establishes early diagnosis of esophageal cancer in patients with primary head and neck cancer. *Am J Gastroenterol*. 2005;100:275-82.
15. Connor MJ, Sharma P. Chromoendoscopy and magnification endoscopy for diagnosing esophageal cancer and dysplasia. *Thorac Surg Clin*. 2004;14(1):87-94.
16. Yoshida Y, Goda K, Tajiri H, Urashima M, Yoshimura N, Kato T. Assessment of Novel Endoscopic Techniques for Visualizing Superficial Esophageal Squamous Cell Carcinoma: Autofluorescence and Narrow-band Imaging. *Dis Esophagus*. 2009;22(5):439-46.
17. Freitag CP, Barros SG, Kruel CD, et al. Esophageal dysplasias are detected by endoscopy with Lugol in patients at risk for squamous cell carcinoma in southern Brazil. *Dis Esophagus*. 1999;12(3):191-5.

18. Sampliner RE. Updated guidelines for the diagnosis, surveillance, and therapy of Barrett's esophagus. *Am J Gastroenterol*. 2002;97(8):1888-95.

19. Katz D, Rothstein R, Schned A, Dunn J, Seaver K, Antonioli D.. The development of dysplasia and adenocarcinoma during endoscopic surveillance of Barrett's esophagus. *Am J Gastroenterol*. 1998;93(4):536-41.

20. Vieth M, Ell C, Gossner L, May A, Stolte M. Histological analysis of endoscopic resection specimens from 326 patients with Barrett's esophagus and early neoplasia. *Endoscopy*. 2004;36(9):776-81.

21. Deinert K, Kiesslich R, Vieth M, Neurath MF, Neuhaus H. In-vivo microvascular imaging of early squamous-cell cancer of the esophagus by confocal laser endomicroscopy. *Endoscopy*. 2007;39(4):366-8.

22. Liu H, Li YQ, Yu T, et al. Confocal laser endomicroscopy for superficial esophageal squamous cell carcinoma. *Endoscopy*. 2009;41(2):99-106.

23. Iguchi Y, Niwa Y, Miyahara R et al. Pilot study on confocal endomiroscopy for determination of the depth of squamous cell esophageal cancer in vivo. *J Gas Hep.* 2009;24:1733-1739.

24. Pech O, Rabenstein T, Manner H, et al. Confocal laser endomicroscopy for in vivo diagnosis of early squamous cell carcinoma in the esophagus. *Clin Gastroenterol Hepatol.* 2008;6(1):89-94.

25. Kiesslich R, Gossner L, Goetz M, et al. In vivo histology of Barrett's esophagus and associated neoplasia by confocal laser endomicroscopy. *Clin Gastroenterol Hepatol*. 2006;4(8):979-87.

26. Pohl H, Rösch T, Vieth M, et al. Miniprobe confocal laser microscopy for the detection of invisible neoplasia in patients with Barrett's oesophagus. *Gut.* 2008;57(12):1648-53.
27. Gaddam S, Mathur SC, Singh M, et al. Novel probe-based confocal laser endomicroscopy criteria and interobserver agreement for the detection of dysplasia in Barrett's esophagus. *Am J Gastroenterol*. 2011;106(11):1961-9.
28. Wallace MB, Sharma P, Lightdale C, et al. Preliminary accuracy and interobserver agreement for the detection of intraepithelial neoplasia in Barrett's esophagus with probe-based confocal laser endomicroscopy. *Gastrointest Endosc*. 2010;72(1):19-24.
29. Dunbar KB, Okolo P 3rd, Montgomery E, Canto MI. Confocal laser endomicroscopy in Barrett's esophagus and endoscopically inapparent Barrett's neoplasia: a prospective, randomized, double-blind, controlled, crossover trial. *Gastrointest Endosc*. 2009;70(4):645-54.
30. Sharma P, Meining AR, Coron E, et al. Real-time increased detection of neoplastic tissue in Barrett's esophagus with probe-based confocal laser endomicroscopy: final results of an international multicenter, prospective, randomized, controlled trial. *Gastrointest Endosc*. 2011;74(3):465-72.
31. Bertani H, Frazzoni M, Dabizzi E, et al. mproved detection of incident dysplasia by probe-based confocal laser endomicroscopy in a Barrett's esophagus surveillance program. *Dig Dis Sci*. 2013;58(1):188-93.
32. Muldoon TJ, Pierce MC, Nida DL, Williams MD, Gillenwater A, Richards-Kortum R. Subcellular-resolution molecular imaging within living tissue by fiber microendoscopy. *Opt Express*. 2007;15(25):16413-23.

33. Muldoon TJ, Anandasabapathy S, Maru D, Richards-Kortum R. High-resolution imaging in Barrett's esophagus: a novel, low-cost endoscopic microscope. *Gastrointest Endosc*. 2008;68(4):737-44.

34. Muldoon TJ, Thekkek N, Roblyer D, et al. Evaluation of quantitative image analysis criteria for the high-resolution microendoscopic detection of neoplasia in Barrett's esophagus. *J Biomed Opt*. 2010;15(2):026027.

35. Pierce MC, Vila PM, Polydorides AD, Richards-Kortum R, Anandasabapathy S. Low-cost endomicroscopy in the esophagus and colon. *Am J Gastroenterol*. 2011;106(9):1722-4.

36. Vila PM, Kingsley MJ, Polydorides AD, et al. Accuracy and interrater reliability for the diagnosis of Barrett's neoplasia among users of a novel, portable high-resolution microendoscope. *Dis Esophagus*. 2013. doi: 10.1111/dote.12040.

37. Siegel R, Naishadham D, Jemal A. Cancer statistics, 2013. *CA Cancer J Clin*. 2013;63(1):11-30.

38. Howlader N, Noone AM, Krapcho M, et al. SEER cancer statistics review, 1975-2009 (Vintage 2009 Populations), National Cancer Institute. Bethesda, MD, http://seer.cancer.gov/csr/1975_2009_pops09/, based on November 2011 SEER data submission, posted to the SEER web site, April 2012. Accessed March 20, 2013.

39. Aghcheli K, Marjani H-A, Nasrollahzadeh D, et al. Prognostic factors for esophageal squamous cell carcinoma—a population-based study in Golestan province, Iran, a high incidence area. *PLoS One*. 2011;6(7):e22152.

40. Rosbach KJ, Shin D, Muldoon TJ, et al. High-resolution fiber optic microscopy with fluorescent contrast enhancement for the identification of axillary lymph node metastases in breast cancer: a pilot study. *Biomed Opt Express*. 2010;1(3):911-922.
41. Quinn MK, Bubi TC, Pierce MC, Kayembe MK, Ramogola-Masire D, Richards-Kortum R. High-resolution microendoscopy for the detection of cervical neoplasia in low-resource settings. *PLoS One*. 2012;7(9):e44924.
42. Pierce MC, Guan Y, Quinn MK, et al. A pilot study of low-cost, high-resolution microendoscopy as a tool for identifying women with cervical precancer. *Cancer Prev Res (Phila)*. 2012;5(11):1273-1279.
43. Muldoon TJ, Roblyer D, Williams MD, Stepanek VM, Richards-Kortum R, Gillenwater AM. Noninvasive imaging of oral neoplasia with a high-resolution fiber-optic microendoscope. *Head Neck*. 2012;34(3):305-312.
44. Aslanoglu M. Electrochemical and spectroscopic studies of the interaction of proflavine with DNA. *Anal Sci*. 2006;22(3):439-443.
45. Schlemper RJ, Riddell RH, Kato Y, et al. The Vienna classification of gastrointestinal epithelial neoplasia. *Gut*. 2000;47(2):251-255.
46. Pierce M, Yu D, Richards-Kortum R. High-resolution fiber-optic microendoscopy for in situ cellular imaging. *J Vis Exp*. 2011;(47):2306.
47. Han JH, Lee J, Kang JU. Pixelation effect removal from fiber bundle probe based optical coherence tomography imaging. *Opt Express*. 2010;18(7):7427-7439.
48. Moraca RJ, Low DE. Outcomes and health-related quality of life after esophagectomy for high-grade dysplasia and intramucosal cancer. *Arch Surg*. 2006;141(6):545–549; discussion 549-51.

49. Gómez V, Buchner AM, Dekker E, et al. Interobserver agreement and accuracy among international experts with probe-based confocal laser endomicroscopy in predicting colorectal neoplasia. *Endoscopy*. 2010;42(4):286-291.

50. van den Broek FJ, van Es JA, van Eeden S, et al. Pilot study of probe-based confocal laser endomicroscopy during colonoscopic surveillance of patients with longstanding ulcerative colitis. *Endoscopy*. 2011;43(2):116-122.

51. Downs-Kelly E, Mendelin JE, Bennett AE, et al. Poor interobserver agreement in the distinction of high-grade dysplasia and adenocarcinoma in pretreatment Barrett's esophagus biopsies. *Am J Gastroenterol*. 2008;103(9):2333–2340.

52. Wang KK, Sampliner RE. Updated guidelines 2008 for the diagnosis, surveillance and therapy of Barrett's esophagus. *Am J Gastroenterology*. 2008;103:788-797.

53. Reid BJ, Blount P, Feng Z, et al. Optimizing endoscopic biopsy detection of early cancers in Barrett's high-grade dysplasia. *Am J Gastroenterol*. 2000;95:3089–96.

54. Ljungqvist MG, Nielsen ME, Ersbøll BK, Frosch S. Image analysis of pellet size for a control system in industrial feed production. *PLoS One*. 2011;6(10):e26492.

55. Pierce MC, Schwarz RA, Bhattar VS, et al. Accuracy of in vivo multimodal optical imaging for detection of oral neoplasia. *Cancer Prev Res (Phila)*. 2012;5(6):801-9.

56. Dromard T, Ravaine V, Ravaine S, Lévêque JL, Sojic N. Remote in vivo imaging of human skin corneocytes by means of an optical fiber bundle. *Rev Sci Instrum*. 2007;78(5):053709.

57. Lane PM, Lam S, McWilliams A, Leriche JC, Anderson MW, Macaulay CE. Confocal fluorescence microendoscopy of bronchial epithelium. *J Biomed Opt*. 2009;14(2):024008.

58. Carlson K, Pavlova I, Collier T, Descour M, Follen M, Richards-Kortum R. Confocal microscopy: imaging cervical precancerous lesions. *Gynecol Oncol*. 2005;99(3 Suppl 1):S84-8.

59. Jean F, Bourg-Heckly G, Viellerobe B. Fibered confocal spectroscopy and multicolor imaging system for in vivo fluorescence analysis. *Opt Express*. 2007;15(7):4008-17.

60. Dubaj V, Mazzolini A, Wood A, Harris M. Optic fibre bundle contact imaging probe employing a laser scanning confocal microscope. *J Microsc*. 2002;207(Pt 2):108-17.

61. Laemmel E, Genet M, Le Goualher G, Perchant A, Le Gargasson JF, Vicaut E. Fibered confocal fluorescence microscopy (Cell-viZio) facilitates extended imaging in the field of microcirculation. A comparison with intravital microscopy. *J Vasc Res*. 2004 Sep-Oct;41(5):400-11.

62. Zhong W, Celli JP, Rizvi I, et al. (2009) In vivo high-resolution fluorescence microendoscopy for ovarian cancer detection and treatment monitoring. *Br J Cancer*. 2009;101(12):2015-22.

63. Roblyer D, Richards-Kortum R, Sokolov K, et al. Multispectral optical imaging device for in vivo detection of oral neoplasia. *J Biomed Opt*. 2008;13(2):024019

64. Rodriguez WR, Christodoulides N, Floriano PN, et al. A microchip CD4 counting method for HIV monitoring in resource-poor settings. *PLoS Med*. 2005;2(7):e182.

65. Moon S, Keles HO, Ozcan A, et al. Integrating microfluidics and lensless imaging for point-of-care testing. *Biosens Bioelectron*. 2009;24(11):3208-14.

66. Chen Y, Xiong T, Yu L, Zeng S, Luo Q. Whole-body Fluorescent Optical Imaging Based on Power Light Emitting Diode. *Conf Proc IEEE Eng Med Biol Soc*. 2005;2:1442-5.

67. Ghoghawala SY, Mannis MJ, Murphy CJ, Rosenblatt MI, Isseroff RR. Economical LED based, real-time, in vivo imaging of murine corneal wound healing. *Exp Eye Res*. 2007 Jun;84(6):1031-8.

68. Han B, Jung B, Nelson JS, Choi EH. Analysis of facial sebum distribution using a digital fluorescent imaging system. *J Biomed Opt*. 2007;12(1):014006.

69. Carlson AL, Hoffmeyer MR, Wall KM, Baugher PJ, Richards-Kortum R, Dharmawardhane SF. In situ analysis of breast cancer progression in murine models using a macroscopic fluorescence imaging system. *Lasers Surg Med*. 2006;38(10):928-38.

70. Alfaro L, Roca MJ. Portable telepathology: methods and tools. *Diagn Pathol*. 2008;3 Suppl 1:S19.

71. Collier T, Guillaud M, Follen M, Malpica A, Richards-Kortum R. Real-time reflectance confocal microscopy: comparison of two-dimensional images and three-dimensional image stacks for detection of cervical precancer. *J Biomed Opt*. 2007;12(2):024021.

72. Martinez AW, Phillips ST, Carrilho E, Thomas SW 3rd, Sindi H, Whitesides GM. Simple telemedicine for developing regions: Simple telemedicine for developing regions: camera phones and paper-based microfluidic devices for real-time, off-site diagnosis. *Anal Chem*. 2008;80(10):3699-707.

73. Massone C, Hofmann-Wellenhof R, Ahlgrimm-Siess V, Gabler G, Ebner C, Soyer HP. Melanoma screening with cellular phones. *PLoS One*. 2007;2(5):e483.

74. Ebner C, Wurm EM, Binder B, et al. Mobile teledermatology: a feasibility study of 58 subjects using mobile phones. *J Telemed Telecare*. 2008;14(1):2-7.

75. Breslauer DN, Maamari RN, Switz NA, Lam WA, Fletcher DA. Mobile phone based clinical microscopy for global health applications. *PLoS One*. 2009;4(7):e6320.

76. Mäkinen J, Keränen K, Hakkarainen J, et al. Inmould integration of a microscope add-on system to a 1.3 Mpix camera phone. *Proc. of SPIE.* 2007;6585:658507.

77. Pérez MA, Mera M, Arias JR, et al. PocketELISA: A low-cost portable ELISA reader based on image analysis over PDA platform for clinical diagnose in medical veterinary. *IEEE International Symposium on Industrial Electronics.* 2008;939-943.

78. Polglase AL, McLaren WJ, Skinner SA, Kiesslich R, Neurath MF, Delaney PM. A fluorescence confocal endomicroscope for in vivo microscopy of the upper- and the lower-GI tract. *Gastrointest Endosc.* 2005;62(5):686-95.

79. Janssen PA, Selwood BL, Dobson SR, Peacock D, Thiessen PN. To dye or not to dye: a randomized, clinical trial of a triple dye/alcohol regime versus dry cord care. *Pediatrics*. 2003;111(1):15-20.

80. McConnell T, Lee C, Couillard M, Sherill W. Trends in umbilical cord care: Scientific evidence for practice. *Newborn Infant Nurs Rev*. 2004;4:211–222.

81. Maisels MJ, McDonagh AF. Phototherapy for neonatal jaundice. *N Engl J Med.* 2008;358(9):920-8.

82. Kaufman RH, Adam E, Mirkovic RR, Melnick JL, Young RL. Treatment of genital herpes simplex virus infection with photodynamic inactivation. *Am J Obstet Gynecol*. 1978;132(8):861-9.

83. Kurman RJ. *Blaustein's pathology of the female genital tract*. 4th ed. New York, NY: Springer-Verlag; 1994.

84. Guillaud M, Cox D, Adler-Storthz K, et al. Exploratory analysis of quantitative histopathology of cervical intraepithelial neoplasia: objectivity, reproducibility, malignancy-associated changes, and human papillomavirus. *Cytometry A*. 2004;60(1):81-9.

85. Collier T, Lacy A, Richards-Kortum R, Malpica A, Follen M. Near real-time confocal microscopy of amelanotic tissue: detection of dysplasia in ex vivo cervical tissue. *Acad Radiol.* 2002;9(5):504-12.

86. The DAVE (Digital Atlas of Video Education) Project. 2010. Available: http://www.daveproject.org.